The Astrophysical Journal, 738:18 (20pp), 2011 September 1 doi:10.1088/0004-637X/738/1/18

TWO COMPONENTS OF THE SOLAR CORONAL EMISSION REVEALED BY EXTREME-ULTRAVIOLET SPECTROSCOPIC OBSERVATIONS

Hui Tian[1], Scott W. McIntosh[1], Bart De Pontieu[2], Juan Martínez-Sykora[2,3], Marybeth Sechler[1], and Xin Wang[4]
[1] High Altitude Observatory, National Center for Atmospheric Research, Boulder, CO 80307, USA; htian@ucar.edu
[2] Lockheed Martin Solar and Astrophysics Laboratory, Palo Alto, CA 94304, USA
[3] Institute of Theoretical Astrophysics, University of Oslo, Blindern, N-0315 Oslo, Norway
[4] School of Earth and Space Sciences, Peking University, 100871 Beijing, China
Received 2011 May 11; accepted 2011 June 6; published 2011 August 9

ABSTRACT

Recent spectroscopic observations have revealed the ubiquitous presence of blueward asymmetries of emission lines formed in the solar corona and transition region. These asymmetries are most prominent in loop footpoint regions, where a clear correlation of the asymmetry with the Doppler shift and line width determined from the single-Gaussian fit is found. Such asymmetries suggest at least two emission components: a primary component accounting for the background emission and a secondary component associated with high-speed upflows. The latter has been proposed to play a vital role in the coronal heating process and there is no agreement on its properties. Here we slightly modify the initially developed technique of red–blue (RB) asymmetry analysis and apply it to both artificial spectra and spectra observed by the Extreme-ultraviolet Imaging Spectrometer on board *Hinode*, and demonstrate that the secondary component usually contributes a few percent of the total emission, and has a velocity ranging from 50 to 150 km s^{-1} and a Gaussian width comparable to that of the primary one in loop footpoint regions. The results of the RB asymmetry analysis are then used to guide a double-Gaussian fit and we find that the obtained properties of the secondary component are generally consistent with those obtained from the RB asymmetry analysis. Through a comparison of the location, relative intensity, and velocity distribution of the blueward secondary component with the properties of the upward propagating disturbances revealed in simultaneous images from the Atmospheric Imaging Assembly on board the *Solar Dynamics Observatory*, we find a clear association of the secondary component with the propagating disturbances.

Key words: line: profiles – solar wind – Sun: corona – Sun: UV radiation

Online-only material: animation, color figures

1. INTRODUCTION

Extreme-ultraviolet (EUV) spectroscopic observations often reveal patches of blueshifted emission at boundaries of some active regions (ARs; Marsch et al. 2004, 2008; Harra et al. 2008; Del Zanna 2008; Doschek et al. 2008; Tripathi et al. 2009; Murray et al. 2010; Brooks & Warren 2011; Warren et al. 2011; Del Zanna et al. 2011). These authors used a single-Gaussian fit to approximate coronal emission line profiles and derived a blueshift of the order of 20 km s^{-1}. Large line widths have also been found in these blueshifted regions (e.g., Doschek et al. 2008). There are suggestions that these blueshifts are indicators of the nascent slow solar wind (Sakao et al. 2007; Harra et al. 2008; Doschek et al. 2008; Brooks & Warren 2011).

Recent investigations have revealed the ubiquitous presence of blueward asymmetries of emission lines formed in the solar corona and transition region (e.g., De Pontieu et al. 2009; McIntosh & De Pontieu 2009b). The enhancement in the blue wings of line profiles is most prominent in loop footpoint regions, such as AR boundaries (Hara et al. 2008; De Pontieu et al. 2009; De Pontieu & McIntosh 2010; McIntosh & De Pontieu 2009a; Peter 2010; Bryans et al. 2010; Tian et al. 2011a; Ugarte-Urra & Warren 2011). The discovery of these asymmetric line profiles suggests the presence of a highly blueshifted (much larger than 20 km s^{-1}) emission component in addition to the primary emission component, and thus provides a significant challenge to previous results and interpretations which are based on a single-Gaussian fit.

De Pontieu et al. (2009) and McIntosh & De Pontieu (2009b) suggested that this secondary emission component is associated with type II spicules (De Pontieu et al. 2007) or rapid blueshifted events (Rouppe van der Voort et al. 2009; De Pontieu et al. 2011) in the chromosphere, and that they play an important role in replenishing the corona with hot plasma (e.g., De Pontieu et al. 2009, 2011; McIntosh & De Pontieu 2009b; Hansteen et al. 2010). The so-called RB (red–blue) asymmetry analysis (De Pontieu et al. 2009; Martínez-Sykora et al. 2011) is based on a comparison of the two wings at same velocity ranges, and detailed analysis indicates that both the speed (50–150 km s^{-1}) and the relative intensity (a few percent of the total emission) of the secondary component are roughly consistent across a temperature range from 100,000 to several million degrees (De Pontieu et al. 2009; McIntosh & De Pontieu 2009b). Through joint imaging and spectroscopic observations of the corona, McIntosh & De Pontieu (2009a) and Tian et al. (2011a) have suggested that the secondary emission component is caused by high-speed repetitive upflows in the form of upward propagating disturbances (PDs) in EUV and X-ray imaging observations. Such disturbances were previously interpreted as slow-mode magnetoacoustic waves (e.g., De Moortel et al. 2000, 2002; Robbrecht et al. 2001; King et al. 2003; McEwan & De Moortel 2006; Marsh et al. 2009, 2011; Wang et al. 2009a, 2009b; De Moortel 2009; Stenborg et al. 2011; Mariska & Muglach 2010) or slow-speed solar wind outflows (e.g., Sakao et al. 2007; He et al. 2010; Guo et al. 2010). There is also a suggestion that they are warps in two-dimensional sheet-like structures (Judge et al. 2011).

Besides the RB asymmetry analysis, the double-Gaussian fit technique has also been used to resolve the second emission

component from line profiles (De Pontieu & McIntosh 2010; Peter 2010; Bryans et al. 2010; Tian et al. 2011a). De Pontieu & McIntosh (2010) and Tian et al. (2011a) applied an RB-guided double-Gaussian fit to spectra with a high signal-to-noise ratio and obvious blueward asymmetry. They used the velocity derived from the RB asymmetry analysis as an initial guess of the velocity of the secondary component. The algorithm undertakes a global minimization of the difference between the observed spectrum and the fit by allowing both primary and secondary component centroids to move by one spectral pixel ($\sim$30 km s^{-1}) to the blue or red of the initial positions. The speed of the secondary component was found to be $\sim$60 km s^{-1} in De Pontieu & McIntosh (2010) and $\sim$100 km s^{-1} in Tian et al. (2011a). They both found that the widths of the two components are similar. The widths of the two Gaussian components were forced to be the same in the double-Gaussian fit algorithm of Bryans et al. (2010), who mentioned that the velocity of the secondary component is often as high as 200 km s^{-1} and that the primary component is also blueshifted by $\sim$10 km s^{-1}. However, they claimed that the double-Gaussian fit is a good approximation for only the Fe XII 195.12 Å and Fe XIII 202.02 Å lines and that other lines are fine with a single-Gaussian fit. By applying a completely free double-Gaussian fit to spectral profiles of the Fe XV 284 Å line, Peter (2010) found that the secondary component usually contributes 10%–20% to the total emission, is usually blueshifted by $\sim$40 km s^{-1}, and is twice as broad as the primary component, especially in loop footpoint regions. However, different settings of initial values and allowable ranges of the seven free parameters can lead to very different fitting results, and thus reasonable initial values and constraints to some free parameters are highly desirable when performing the double-Gaussian fit.

Here we slightly modify the initially developed technique of RB asymmetry analysis and apply it to both artificial and observed spectra by the EUV Imaging Spectrometer (EIS; Culhane et al. 2007) on board *Hinode*, and demonstrate that the speed of the secondary component usually does not reach 200 km s^{-1} and that the widths of the two components are comparable. We then use parameters determined from the RB asymmetry analysis to guide the double-Gaussian fit to each spectrum that is observed to have an obvious blueward asymmetry. Both the RB asymmetry analysis and the double-Gaussian fit yield consistent results. We also use imaging observations simultaneously performed by the Atmospheric Imaging Assembly (AIA; Lemen et al. 2011) on board the *Solar Dynamics Observatory* (*SDO*) to demonstrate that the PDs at AR edges are plasma upflows which are indeed responsible for the blueward asymmetries of line profiles.

2. ARTIFICIAL LINE PROFILES

The technique of RB asymmetry analysis was first introduced by De Pontieu et al. (2009). In our previous work (De Pontieu et al. 2009, 2011; De Pontieu & McIntosh 2010; McIntosh & De Pontieu 2009a, 2009b; McIntosh et al. 2011; Tian et al. 2011a; Martínez-Sykora et al. 2011), we first interpolated the line profile to a spectral resolution 10 times greater than the original one, then subtracted the blue wing emission integrated over a narrow spectral range from that at the same position and over the same range in the red wing. The range of integration was then sequentially stepped outward from the line centroid to build an RB asymmetry profile (simply RB profile). The RB asymmetry for an offset velocity u_c can be expressed as the following (De Pontieu et al. 2009; Martínez-Sykora et al. 2011):

$$\mathrm{RB}(u_c) = \int_{u_c-\delta u/2}^{u_c+\delta u/2} I(u)du - \int_{-u_c-\delta u/2}^{-u_c+\delta u/2} I(u)du, \quad (1)$$

where u_c, δu, and $I(u)$ represent the velocity from the line centroid, the velocity range over which the RB asymmetry is determined, and the spectral intensity, respectively. The value of δu is usually set as 20 km s^{-1}. In our previous work, we used the single-Gaussian fit to determine the line centroid. The resulting RB profile can be normalized to the peak intensity derived from the single-Gaussian fit.

Here we slightly modify this technique by using the spectral position corresponding to the peak intensity as the line centroid. The resulting RB profile is then normalized to the peak intensity of the observed line profile. In the following the RB profiles all refer to normalized RB profiles. The originally defined and modified techniques are designated as RB_S and RB_P, respectively. In the following we apply these two techniques to artificial spectra composed of two Gaussian components to test the ability of the RB asymmetry analysis to resolve the secondary component.

Similar to Martínez-Sykora et al. (2011), each artificial spectrum consists of a fixed primary component and a much weaker secondary component. However, to mimic the observed EIS spectra, the Gaussian parameters we use here are very different from those in Martínez-Sykora et al. (2011). The spectral pixel size is set as 24 km s^{-1}, similar to that of the EIS spectra at around 274 Å. The relative peak intensity of the secondary component with respect to the primary one can be set as any value below 30%, while in Figure 1 we only show the case of 20%. The Gaussian width ($1/e$ width) of the primary component is set to be 56 km s^{-1}, a value comparable to the coronal line width (including instrumental, thermal, and non-thermal width) observed by EIS. For the secondary component, three values of the width are chosen (28, 56, and 112 km s^{-1}). The spectral position of the secondary component is shifted by -20, -40, -60, ..., -180 km s^{-1} with respect to the major component and they are shown as different colors in Figure 1.

After applying the RB_S and RB_P techniques to each artificial spectrum, we obtain RB asymmetry profiles of each spectrum. The same colors are used in the RB asymmetry plots of Figure 1. In the third and fourth rows of Figure 1 we plot the peak intensity, velocity, and $1/e$ width derived from the RB analysis as a function of the velocity offset of the secondary component.

As noticed by Martínez-Sykora et al. (2011), when the width of the secondary component is considerably smaller (28 km s^{-1}) than that of the primary one and the secondary component is centered at velocities lower than the Gaussian width of the primary component, the RB_S asymmetry profile is blueward at low velocities and redward at higher velocities. The asymmetry profile reverses when the offset velocity of the secondary component is larger than the width of the primary component. Here we find that the RB_P asymmetry profile is redward at low velocities and blueward at higher velocities when the secondary component is too close to the primary one. As the offset velocity increases to a value larger than the width of the primary component, the RB_P asymmetry profile is blueward at all velocities. We find that when the velocity offset is larger than the width of the primary component, the velocity, width, and relative intensity derived from the RB_P technique are very close to the true velocity and width of the secondary component. The RB_S technique does slightly worse but still can give relatively accurate values of the parameters.

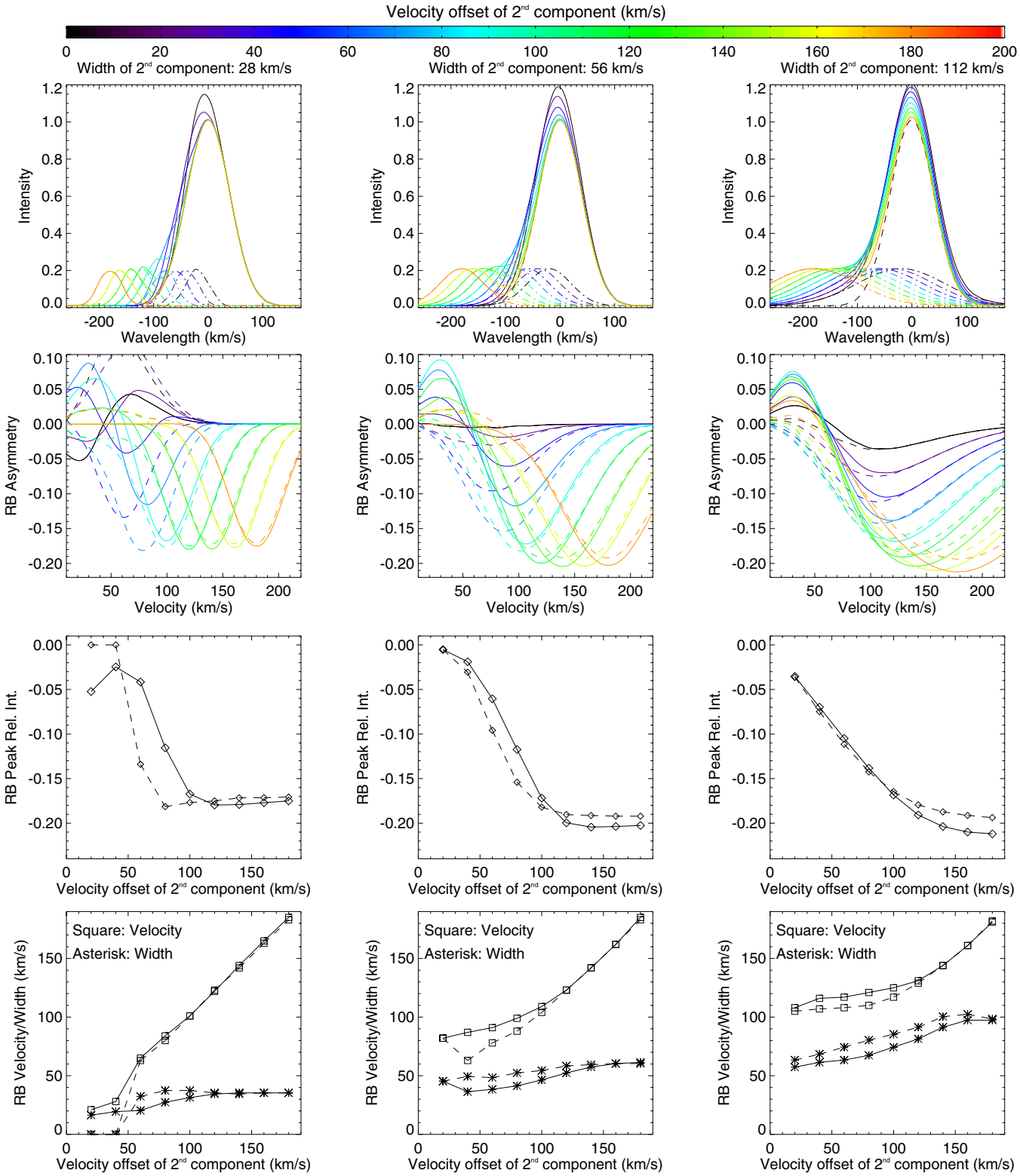

Figure 1. Parameters derived from the RB asymmetry profiles of artificial emission line profiles. First row: the primary, secondary, and total emission profiles are shown as the dashed, dash-dotted, and solid lines, respectively. The peak intensity of the secondary component is set as 20% of that of the primary one. Second row: RB_S (solid) and RB_P (dashed) asymmetry profiles. Different colors represent different velocity offsets of the secondary component. Third row: the relative intensity of the peak of the asymmetry profile. Fourth row: the velocity and $1/e$ width of the asymmetry profile. Solid and dashed lines represent results of RB_S and RB_P, respectively. The Gaussian width of the secondary component is 28, 56, and 112 km s^{-1} for the left, middle, and right columns, respectively.

(A color version of this figure is available in the online journal.)

When the widths of two components are the same (56 km s^{-1}), no matter where the secondary component is centered, the RB_S asymmetry profile is redward at low velocities and blueward at higher velocities, and the RB_P asymmetry profile is blueward at all velocities. By comparing the velocity, width, and relative intensity derived from the RB techniques with the true

parameters of the secondary component, we can still conclude that the RB techniques can provide a relatively accurate estimate of the properties of the secondary component provided the offset velocity is larger than the width of the primary component. We notice that compared to the RB_S technique, the RB_P technique has a better ability to reproduce the parameters of the secondary component, especially when the offset velocity is smaller than twice the width of the primary component. The improvement is around 10 km s^{-1} in the velocity and width, and 4% in the relative intensity.

When the secondary component is considerably broader (112 km s^{-1}) than that of the primary one, the RB profiles show morphologies similar to the case of 56 km s^{-1}. However, both the RB_S and RB_P techniques cannot reproduce an offset velocity smaller than 100 km s^{-1}. The velocity derived from RB analysis is always larger than 100 km s^{-1} if the secondary component is twice as broad as the primary one. There is also a large discrepancy between the width derived from RB analysis and the true width of the secondary component if the offset velocity is smaller than twice the width of the primary component (112 km s^{-1}).

We notice that in each of the three cases, the RB techniques can give an extremely accurate estimate of the velocity when the offset velocity of the secondary component is larger than 112 km s^{-1}.

We have varied the intensity ratio of the two components in the range of 5%–30% and obtain basically the same results, except for the different values of the calculated relative intensities. One thing we have noticed from Figure 1 is that the RB technique tends to underestimate the value of the relative intensity of the secondary component at smaller offset velocities (e.g., 56–112 km s^{-1}). This is especially the case for the RB_S technique which we used in our previous work. From the third row of Figure 1, we can see that in the velocity range of ∼56–112 km s^{-1} the relative intensity of the secondary component recovered from the RB_P technique is much closer to the real value (−0.20 in Figure 1), as compared to the RB_S technique. The underestimation of relative intensity might be improved by using the χ^2 method (Martínez-Sykora et al. 2011).

The fact that the calculated RB velocities and relative intensities obviously deviate from the real values when the offset velocities of the secondary component are smaller than the width of the primary component has an important implication for the development of future EUV spectrographs. The EIS instrument has a large instrumental width of ∼35 km s^{-1} (e.g., Doschek et al. 2007), which contributes almost half of the total line width. The Interface Region Imaging Spectrograph (IRIS), which is scheduled to be launched at the end of 2012, will have a much smaller instrumental width (a Gaussian width of ∼5 km s^{-1} at 1400 Å) and our RB technique should be able to accurately resolve the secondary component at smaller offset velocities. The very high spectral resolution (∼3 km s^{-1}) of the IRIS spectrograph will greatly reduce the error caused by the interpolation of line profiles.

In the following we pick out two ARs and investigate properties of the secondary component from the spectra obtained by EIS. Since the modified RB technique, RB_P, has a better ability to accurately resolve the blueshifted secondary component as compared to the originally defined RB_S technique, here we mainly present results by applying the RB_P technique instead of the RB_S technique to the real data. A comparison between the RB_P and RB_S results for the 2010 September 16 observation (see the details of this observation in Section 4) is presented in Appendix A.

3. EIS OBSERVATION ON 2007 JANUARY 18

The 1″ × 512″ slit of EIS was used to scan AR NOAA 10938 from 18:12 to 20:27 on 2007 January 18, with an exposure time of 30 s and a step size of 1″. These data were previously analyzed by Hara et al. (2008) and Peter (2010) for the purpose of investigating properties of asymmetric line profiles. Hara et al. (2008) mainly used the Fe XIV 274.20 Å and Fe XV 284.16 Å lines, which are formed around a temperature of 2 MK, while Peter (2010) only focused on the Fe XV 284.16 Å line. Here we choose both lines for our study, but focus on the Fe XIV 274.20 Å line. Peter (2010) mentioned that the Fe XV 284.16 Å line is blended with Al IX 284.03 Å and that the latter usually contributes no more than 5% to the deviation from a single-Gaussian profile. However, as we will discuss later, in some locations the blend can greatly complicate the asymmetries of line profiles. The Fe XIV 274.20 Å line is also a strong line and it is blended with Si VII 274.18 Å. The blend is much weaker than Fe XIV 274.20 Å and can safely be ignored in AR conditions (Young et al. 2007). Moreover, this blend is very close (about one spectral pixel) to the line center of Fe XIV 274.20 Å, and thus it should not have an important influence on the results of our RB asymmetry analysis and Gaussian fit. Further confidence is given by the highly similar behavior of the line moments and profile asymmetries between Fe XIV 274.20 Å and the weaker Fe XIV 264.78 Å line in most ARs we analyzed (see Appendix B), although the Fe XIV 264.78 Å line is usually noisier than Fe XIV 274.20 Å.

The SolarSoft (SSW) routine *eis_prep.pro* was applied to correct and calibrate the EIS data. This includes CCD pedestal and dark current subtraction, cosmic ray removing, warm and hot pixels identification, absolute calibration, error estimation, and so on. The effects of slit tilt and orbital variation (thermal drift) were estimated by using the SSW routine *eis_wave_corr.pro* and removed from the data. After that, a running average over five pixels along the slit and three pixels across the slit was applied to the spectra to improve the signal-to-noise ratio.

As a common practice, a single-Gaussian fit was applied to each spectrum, and Figures 2(a)–(c) show the spatial distributions of the Gaussian parameters for Fe XIV 274.20 Å. Figure 2(d) shows the map of reduced χ_r^2 for the fit. The reduced χ_r^2 is defined as the following (e.g., Bevington & Robinson 1992; Peter 2001):

$$\chi_r^2 = \sum \frac{1}{N-f} \frac{(d_i - m_i)^2}{\sigma_i^2}, \quad (2)$$

where d_i, m_i, and σ_i denote the observed spectral radiance, fitted spectral radiance, and measurement error calculated by using the SSW routine *eis_prep.pro* (mainly Poisson error), respectively. Here, i represents the spectral position and the summation is performed over all the N spectral positions. The degrees of freedom are given by f and are equal to 4 or 7 for a single- or a double-Gaussian fit, respectively.

We assume zero shift of the profile averaged over the entire observation region. We can see that the loop footpoint regions, or boundaries of the AR, are characterized by a blueshift of ∼20 km s^{-1} and an enhancement of the line width, a well-known phenomenon in the *Hinode* era (e.g., Marsch et al. 2008; Harra et al. 2008; Del Zanna 2008; Doschek et al. 2008; McIntosh & De Pontieu 2009a; Murray et al. 2010; Peter 2010; Tian et al.

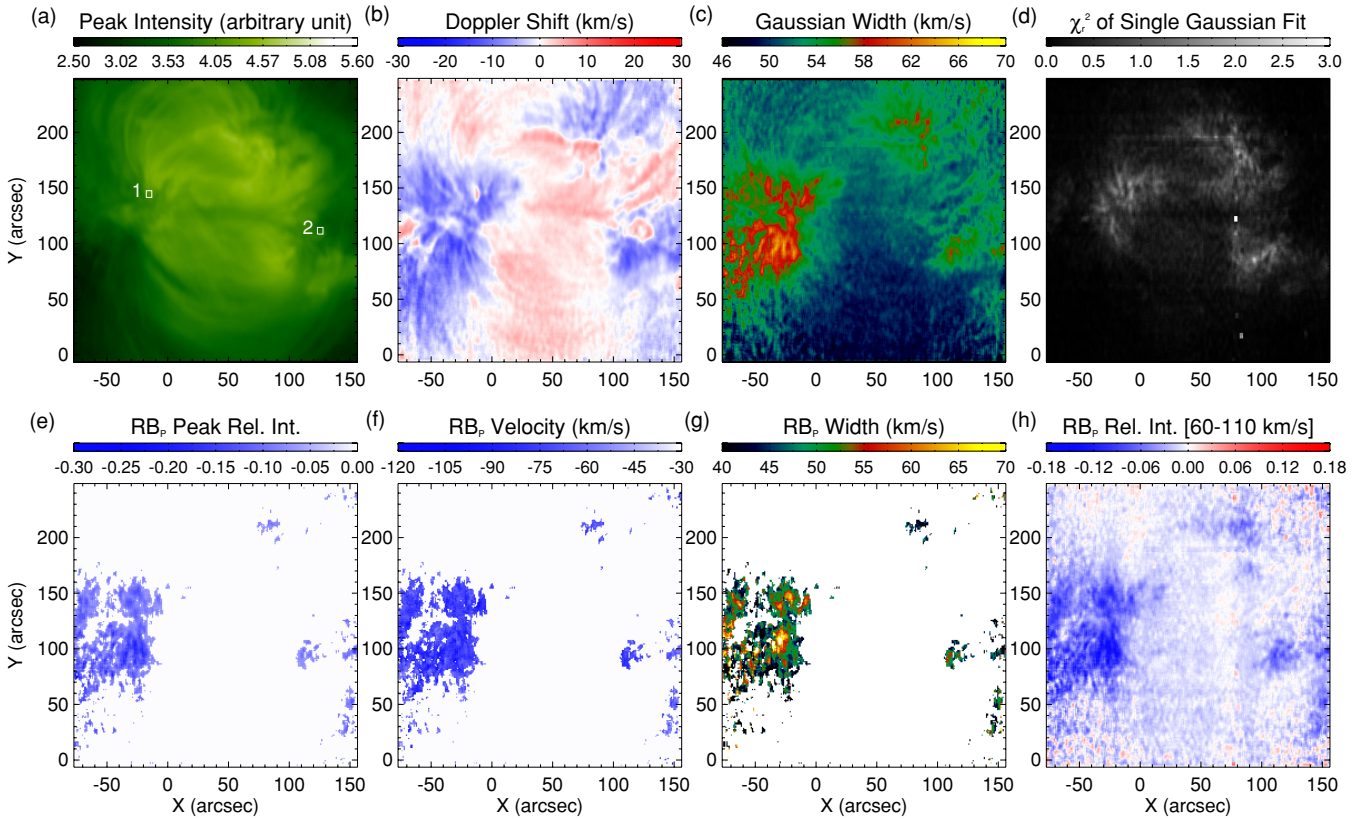

Figure 2. Spatial distributions of the parameters derived from the single-Gaussian fit (a–c) and RB asymmetry analyses (RB_P, e–g) for Fe XIV 274.20 Å. The map of χ_r^2 is shown in (d). The map of the average relative intensity in the velocity interval of 60–110 km s^{-1}, as obtained from the RB profiles, is shown in (h). The two squares in (a) mark the locations where profiles are averaged and presented in Figure 4.

(A color version of this figure is available in the online journal.)

2011a; Brooks & Warren 2011; Warren et al. 2011; Del Zanna et al. 2011). However, the goodness of the fit, the χ_r^2, is also clearly enhanced mainly in loop footpoint regions, indicating an obvious deviation from a single-Gaussian profile there (e.g., Peter 2001, 2010). Note that the definition of χ_r^2 in Peter (2010) is not correct and that it is probably a typographic error.

3.1. RB Asymmetry Analysis

We applied the modified RB technique RB_P to each spectrum and calculated the average relative intensity in the velocity interval of 60–110 km s^{-1} from the RB asymmetry profile. Figure 2(h) shows the spatial distribution of this average RB asymmetry. Here a negative/positive value indicates an enhancement of the blue/red wing in this velocity interval. We can see that the blueward asymmetry is most prominent at loop footpoint regions, generally coincident with the blueshift, width enhancement, and χ_r^2 enhancement. For further analysis, we only selected those locations where this average RB asymmetry is smaller than −0.05 (obvious blueward asymmetry) and the signal-to-noise ratio of the profile (defined as the ratio of the peak and background intensities) is larger than five. We have to mention that such a cutoff excludes the analysis of spectra in the AR core and edges where the magnetic field lines largely incline with respect to the line of sight, since an inclination of the magnetic field line usually leads to a smaller offset velocity of the secondary component in the line-of-sight direction, which would reduce the value of the relative intensity derived from the RB technique (see Figure 1). Figures 2(e)–(g) show the peak relative intensity, velocity, and $1/e$ width derived from RB_P asymmetry profiles at these locations. The distributions of these three parameters are presented as the red histograms in Figures 6(a)–(c).

In Figure 3, we show the scatter plots of the relationship between Doppler shift/Gaussian width derived from the single-Gaussian fit and the peak relative intensity derived from RB_P asymmetry profiles for Fe XIV 274.20 Å. Here only data points with blueshift at those selected locations are shown. A clear correlation is found in each of the two panels in Figure 3. Such a correlation strongly suggests that the clear blueshift and enhanced line width in the loop footpoint regions are related to or caused by the blueward asymmetries. We can simply imagine a faint high-speed upflow superimposed on a strong and almost stationary (or slightly shifted) background in the line of sight. Such a scenario would naturally lead to a blueward asymmetric line profile. And a single-Gaussian fit to the total emission line profile would result in a blueshift and enhanced line width, as compared to the line profile of the background emission—a similar conclusion was reached by Peter (2010), Raju (1999), and Raju et al. (2011). So it is clear that the blueshift at AR boundaries, which was reported in many previous investigations (Marsch et al. 2004, 2008; Harra et al. 2008; Del Zanna 2008; Doschek et al. 2008; Tripathi et al. 2009; Murray et al. 2010; Peter 2010; Brooks & Warren 2011; Warren et al. 2011; Del Zanna et al. 2011; He et al. 2010), is actually a composite effect of at least two emission components and cannot reflect the real physical process (McIntosh & De Pontieu 2009a; De Pontieu & McIntosh 2010; Peter 2010; Bryans et al. 2010; Tian et al. 2011a). Some authors claim that the blueshifts derived from the single-Gaussian fit at AR boundaries are indicators of the nascent slow solar wind (Sakao et al. 2007; Harra et al. 2008;

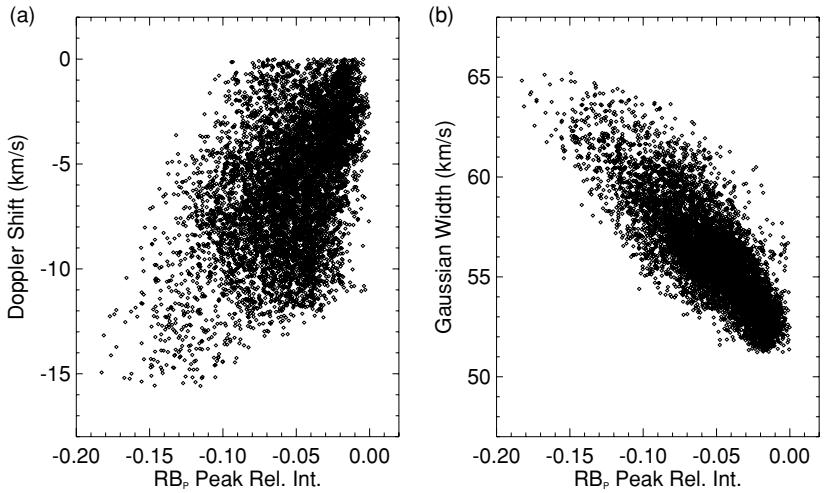

Figure 3. Scatter plots of the relationship between Doppler shift/Gaussian width derived from a single-Gaussian fit and peak relative intensity derived from RB asymmetry analysis (RB$_P$) for Fe XIV 274.20 Å.

Doschek et al. 2008). If this is the case, the wind speed must have been largely underestimated if the source of the mass supply to the solar wind is the secondary component, or overestimated if the primary component dominates the mass supply to the solar wind. Our results also suggest that the enhanced line width can be the result of the superposition of different emission components with different velocities and is not necessarily related to the increase in the Alfvén wave amplitude (Dolla & Zhukov 2011). We think that both the inhomogeneities of flow velocities and Alfvén waves may contribute to the observed non-thermal width of an emission line, and that caution must be taken when interpreting the non-thermal width as purely cased by Alfvén waves (e.g., Banerjee et al. 1998, 2009; Peter 2010).

From Figure 6(a), we can see that the distribution of the intensity ratio (relative intensity of the secondary component) peaks around 0.07 but can reach as high as 0.3. This is generally consistent with the previous result that the blueward excess emission is often a few percent of the total emission, which is based on the RB$_S$ technique (e.g., De Pontieu et al. 2009; McIntosh & De Pontieu 2009b). However, Peter (2010) found a relative intensity of some 10%–20% based on his free double-Gaussian fit.

As mentioned above, when the width of the secondary component is not considerably larger than that of the primary one, the RB$_P$ technique can provide an accurate estimate of the Gaussian parameters of the secondary component provided the offset velocity is larger than the width (~56 km s^{-1}) of the primary component. As seen from Figure 6(b), the RB$_P$ velocity seldom reaches 100 km s^{-1} and its distribution peaks at ~75 km s^{-1}. Such a result would exclude the possibility of a very broad secondary component, as claimed by Peter (2010) based on a free double-Gaussian fit. This is because the velocity derived from RB analysis is always larger than 100 km s^{-1} when the secondary component is twice as broad as the primary one (see Figure 1). In Figure 6(c), we can see that the RB$_P$ width is usually smaller than 60 km s^{-1} and larger than 35 km s^{-1}, and that its distribution peaks around 50 km s^{-1}, which is also not consistent with what we expect if the secondary component is twice as broad as the primary one. From the last panel of Figure 1, we can see that the RB$_P$ width is always larger than 60 km s^{-1} in such a case. From Figure 1 we can also see that when the width of the secondary component is considerably smaller (28 km s^{-1}) than that of the primary one, the RB$_P$ width is always smaller than 35 km s^{-1}, which is not consistent with the observed histogram in Figure 6(c). These inconsistencies strongly suggest that the secondary component cannot be considerably broader or narrower than the primary one. The widths of the two components should be comparable. This conclusion implies that the assumption of the same width of the two components in the double-Gaussian fit algorithm of Bryans et al. (2010) is reasonable.

The velocity distribution presented in Figure 6(b) is not consistent with the scenario of a very high-speed (~200 km s^{-1}) secondary component, as suggested by Bryans et al. (2010) after analyzing another data set. As seen from Figure 1, the velocity derived from the RB$_P$ technique is extremely close to (usually less than 5 km s^{-1}) the true velocity of the secondary component when the latter is larger than 112 km s^{-1}. If very large velocities exist, the RB$_P$ technique should yield such large numbers of velocities. However, the observed velocity derived by using the RB$_P$ technique seldom reaches higher than 150 km s^{-1}, indicating that the velocity of the secondary component in our observation cannot be as high as 200 km s^{-1}. We have to mention that the magnitude of velocity also depends on the viewing angle. However, in loop footpoint regions usually a large portion of the magnetic field lines are almost vertical so that the line-of-sight effect should not be very significant at disk center. We also applied the RB asymmetry analysis to the data analyzed by Bryans et al. (2010) and found larger velocities (~95 km s^{-1}) of the secondary component in that AR (see Appendix C). But still the velocity seldom reaches 200 km s^{-1}.

3.2. Double-Gaussian Fit

Following the initial idea of using the RB$_S$ analysis result to guide a double-Gaussian fit (De Pontieu & McIntosh 2010; Tian et al. 2011a), we designed a similar but modified algorithm. The peak intensity, velocity, and width derived from a single-Gaussian fit were used as the initial guess of those parameters of the primary Gaussian component. The single-Gaussian background was also used as the initial value of the double-Gaussian background. Meanwhile, we used the peak intensity and velocity obtained through the RB$_P$ analysis as the initial values of the same parameters of the secondary Gaussian component. The width of the secondary component was initially set as the same

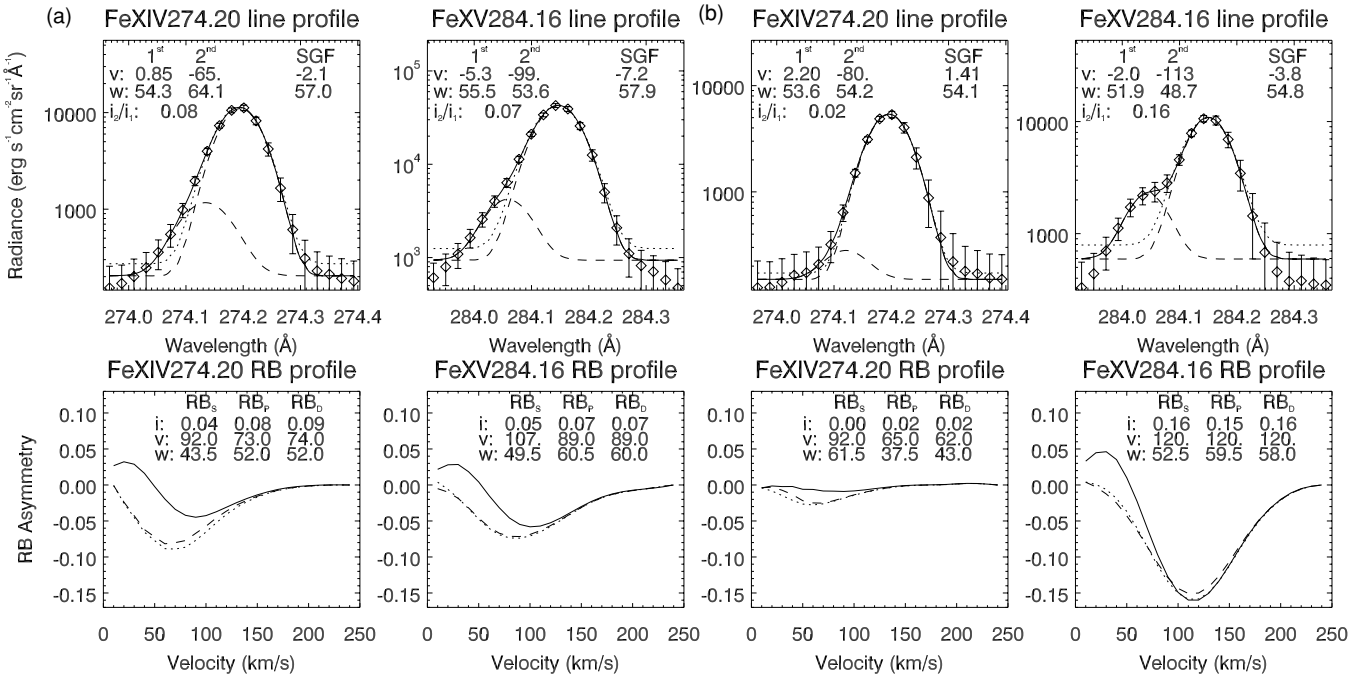

Figure 4. (a) RB asymmetry profiles of the Fe XIV 274.20 Å and Fe XV 284.16 Å line profiles averaged in region 1 marked in Figure 2(a). Top: the observed spectra and measurement errors are shown as the diamonds and error bars, respectively. The dotted lines are single-Gaussian fits. The two dashed lines in each panel represent the two Gaussian components and the solid line is the sum of the two components. The velocity (v) and Gaussian width (w) derived from the single-Gaussian fit (SGF) and double-Gaussian fit (first/second for the two components) are shown in each panel. Also shown is the intensity ratio of the secondary component to the primary one (i_2/i_1). Bottom: the solid, dashed, and dotted lines represent RB profiles for RB_S, RB_P, and RB_D, respectively. The peak relative intensity (i), velocity (v), and $1/e$ width (w) are shown in each panel. (b) Same as (a) but for the line profiles averaged in region 2 marked in Figure 2(a).

as the primary component. During the iterations, we allowed all three intensities (peak intensities of the two components and the background intensity) to vary within the range of 75%–125% of the corresponding initial values. The velocity was allowed to move to the blue or red of the initial position by one spectral pixel (~24 km s^{-1} at 274 Å) for the primary component and two pixels for the secondary component. We also allowed the width to increase or decrease by one spectral pixel for the primary component and two pixels for the secondary component. The algorithm undertook a global minimization of the difference between the observed and fitted spectrum.

We present several examples of the observed and fitted profiles of both the Fe XIV 274.20 Å and Fe XV 284.16 Å lines in Figure 4. The profiles in Figures 4(a) and (b) are the profiles averaged, respectively, over region 1 and 2 marked in Figure 2. By comparing the observed profiles with the different fitting profiles, we can clearly see the better performance of the double-Gaussian fit and the deviations of the observed profiles from the single-Gaussian fits.

After the double-Gaussian fit, we took the velocity of the primary component as the line centroid and calculated the RB asymmetry profile (here RB_D). The lower panels of Figure 4 show the three RB asymmetry profiles (RB_S, RB_P, and RB_D). We can see that RB_P and RB_D show similar behaviors and values of the three parameters are also very close.

It is known that the Fe XV 284.16 Å line is blended with Al IX 284.03 Å (e.g., Young et al. 2007; Brown et al. 2008). The latter is sitting at ~150 km s^{-1} away from the spectral position of Fe XV 284.16 Å so that this blend is potentially contaminating the blue wing of the line and may complicate the RB analysis and Gaussian fit. For example, the line profiles in both Figures 4(a) and (b) were obtained around loop footpoint regions (marked in Figure 2). The magnitude of asymmetry is comparable in both the Fe XIV 274.20 Å and Fe XV 284.16 Å line profiles shown in Figure 4(a), indicating that the blend Al IX 284.03 Å can be ignored. However, in Figure 4(b) we see a ~2% blueward asymmetry in Fe XIV 274.20 Å but a ~16% blueward asymmetry in Fe XV 284.16 Å. Since the two lines have similar formation temperatures, the completely different magnitude of asymmetries in the two lines strongly suggests that the bump at the blue wing of Fe XV 284.16 Å is dominated by the blend Al IX 284.03 Å. Therefore, we focus on the Fe XIV 274.20 Å line instead of Fe XV 284.16 Å, which was used by Peter (2010).

We then apply the RB_P guided Gaussian fit and RB_D analyses to all spectra of Fe XIV 274.20 Å with obvious blueward asymmetries and large signal-to-noise ratio. We present the spatial distributions of the three Gaussian parameters of both components in Figure 5. In addition, the intensity ratio and velocity difference of the two components are also shown in Figure 5. We found that in most locations the primary component is slightly blueshifted (~10 km s^{-1}), a result also found by Bryans et al. (2010), who interpreted it as the nascent slow solar wind from AR boundaries (Wang et al. 2009c). Yet for the secondary component, the velocity is largely blueshifted (~80 km s^{-1}) at almost all locations. The maps of parameters derived from RB_D asymmetry profiles are very similar to those derived from RB_P and thus are not shown here.

Histograms of the intensity ratio (relative intensity), velocity difference (velocity), and Gaussian width of the secondary component as derived from double-Gaussian fit and RB asymmetry analyses (RB_P, RB_D) are presented in Figure 6. We can see that they are very similar, especially RB_P and RB_D. The intensity ratio peaks around 0.07 and can also reach as high as 0.3. For RB_P and RB_D, the velocity and width both have a narrow distribution which peaks at ~75 km s^{-1} and ~50 km s^{-1}, respectively.

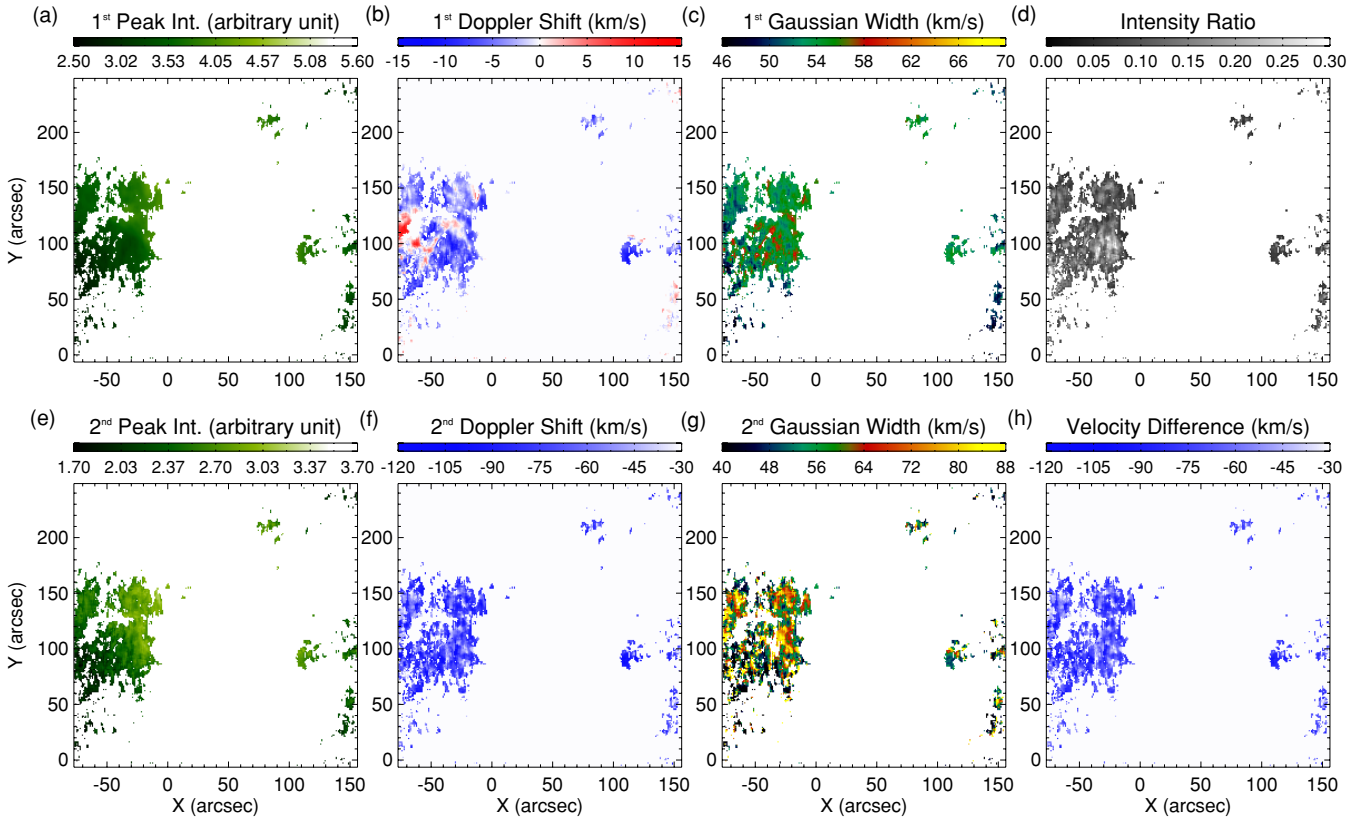

Figure 5. Parameters of the primary (a–c) and secondary (e–g) components as derived from the double-Gaussian fit for Fe XIV 274.20 Å. The intensity ratio and velocity difference of the two components are shown in (d) and (h), respectively.

(A color version of this figure is available in the online journal.)

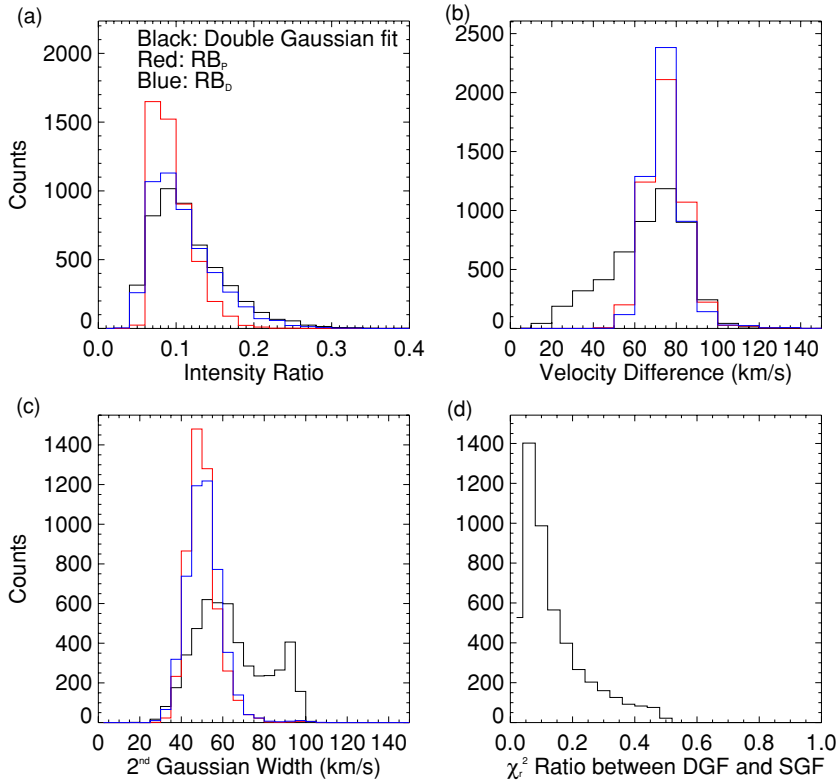

Figure 6. Histograms of the intensity ratio (a), velocity difference (b), and Gaussian width of the secondary component (c), as derived from the double-Gaussian fit (black) and RB asymmetry analyses (red/blue for RB_P/RB_D) for Fe XIV 274.20 Å. Panel (d) shows the histograms of the χ_r^2 ratio between the double- and single-Gaussian fits.

(A color version of this figure is available in the online journal.)

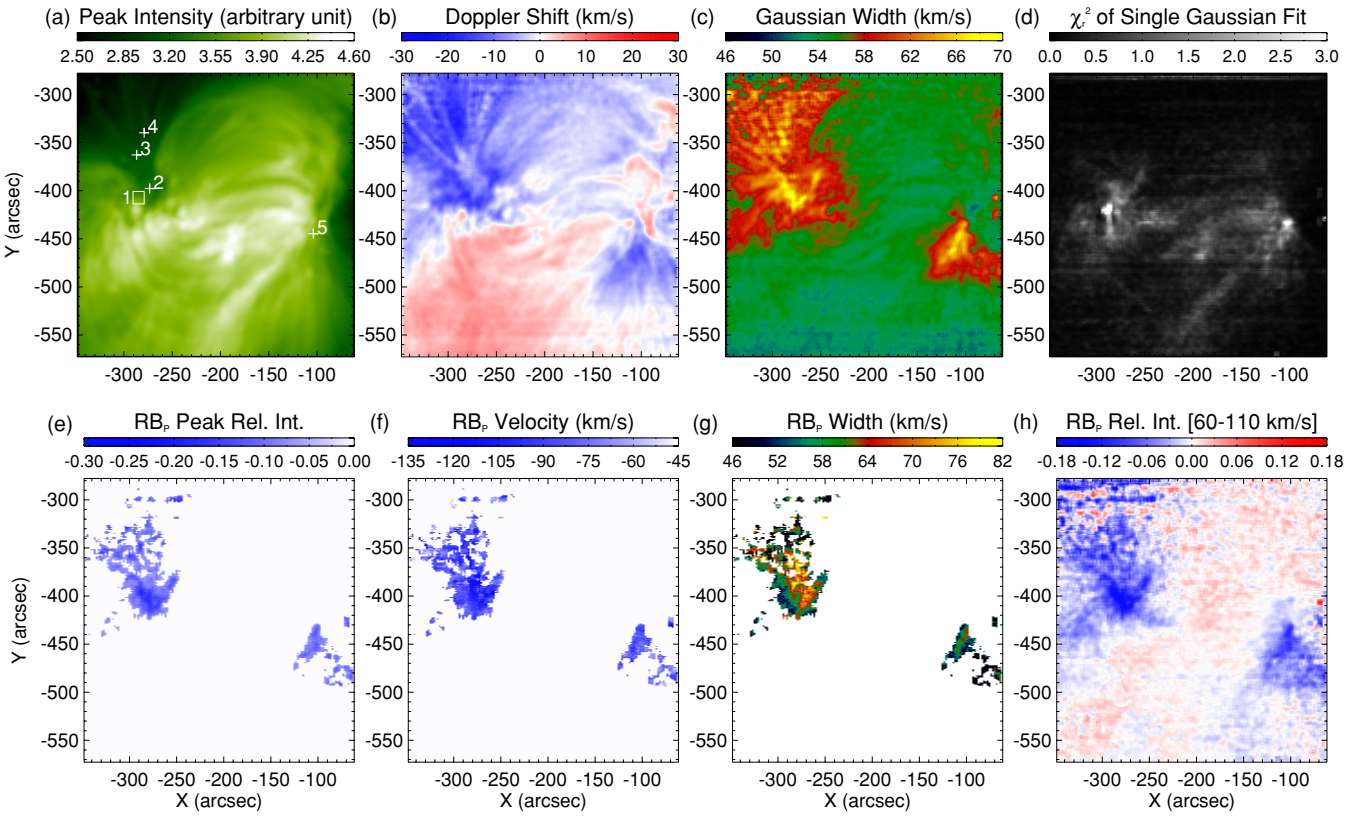

Figure 7. Same as Figure 2 but for the observation on 2010 September 16. The square in (a) marks the location where profiles of several emission lines are averaged and presented in Figure 9(a). The four pluses mark locations of the Fe XIV 274.20 Å line profiles presented in Figures 9(b)–(e).

(A color version of this figure is available in the online journal.)

However, for the double-Gaussian fit, most of the width values are still much smaller than ~100 km s^{-1} and the width distribution peaks slightly higher. The velocity difference is usually in the range of 50–100 km s^{-1}, but the double-Gaussian fit algorithm also produces some relatively small values of velocity difference (10–50 km s^{-1}). However, these relatively small blueshifts are found at only a few locations and they are not prevalent.

The χ_r^2 value of the double-Gaussian fit is usually smaller than unity—a similar result was also found by Peter (2010), who attributed it to the overestimation of the measurement error. From Figure 6(d), we can see that the χ_r^2 ratio between the double- and single-Gaussian fits is usually less than 0.5 in the regions characteristic of obvious blueward asymmetries. Such a result indicates that the double-Gaussian fit does at least two times better than the single-Gaussian fit for these asymmetric line profiles. It is likely that even more components, e.g., a component from cooling downflows, might be present in the observed emission. However, a reliable decomposition of these additional components cannot be made due to the relatively large instrumental width and modest spectral resolution of EIS. With the upcoming IRIS data, we may be able to resolve more coronal emission components.

4. EIS AND AIA OBSERVATIONS ON 2010 SEPTEMBER 16

The other observation was performed by EIS on 2010 September 16, with simultaneous observations by AIA. The EIS instrument scanned NOAA AR 11106 from 10:38 to 11:57 UT. The 2″ × 512″ slit was used for the observation, with a 60 s exposure. After standard correction and calibration of the EIS data, a running average over five pixels along the slit and three pixels across the slit was applied to the spectra to improve the signal-to-noise ratio. Four relatively strong and clean emission lines in the spectral window were selected for our study: Si VII 275.35 Å, Si X 258.37 Å, Fe XIII 202.04 Å, and Fe XIV 274.20 Å. Their formation temperatures are $\log(T/\mathrm{K}) = 5.8$, 6.1, 6.2, and 6.3, respectively (Young et al. 2007). But we will mainly concentrate on the hottest strong line, Fe XIV 274.20 Å.

A single-Gaussian fit was first applied to each spectrum to derive the line intensity, centroid, and Gaussian width. By assuming that the average Doppler shift of each line is zero over the entire region, we calculated the Doppler shift from the line centroid for each spectral profile. Maps of the Gaussian parameters and χ_r^2 for Fe XIV 274.20 Å are presented in Figures 7(a)–(d). Again, we clearly see that the loop footpoint regions, or boundaries of the AR, are characterized by a blueshift of ~20 km s^{-1} and an enhancement of the line width. The deviation from a single-Gaussian profile, which is quantified by the enhancement of χ_r^2, is also clearly seen in the loop footpoint regions. The Si X 258.37 Å and Fe XIII 202.04 Å lines reveal basically the same structures in the maps of Gaussian parameters. The cool line Si VII 275.35 Å shows prominent redshifts in the fan regions (not shown here), a phenomenon found also by Warren et al. (2011). Such redshifts could be the downflows after cooling of the high-speed upflows and evidence for the mass circulation in coronal loops (Marsch et al. 2008).

4.1. RB Asymmetry Analysis

Similar to before, we applied the RB$_P$ technique to each spectrum and calculated the average relative intensity in the

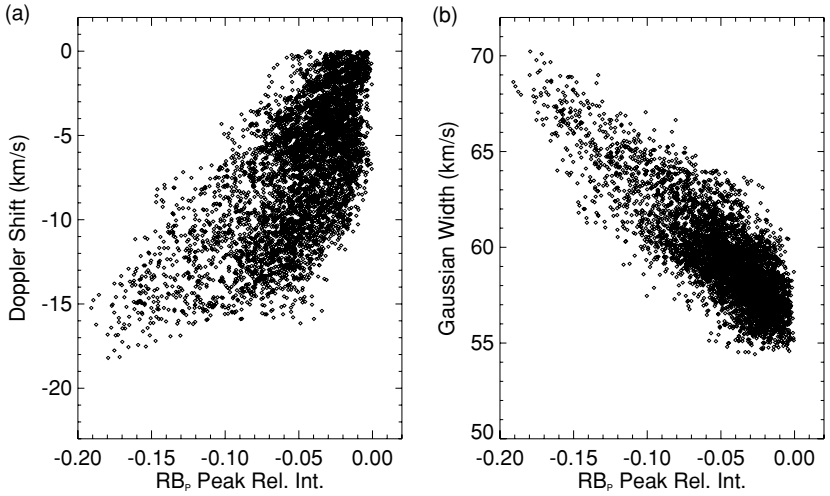

Figure 8. Same as Figure 3 but for the observation on 2010 September 16.

velocity interval of 60–110 km s^{-1} from the RB asymmetry profile. Figure 7(h) shows the spatial distribution of this average RB asymmetry. It is clear that the blueward asymmetry is most prominent at the two edges of the AR, generally coincident with the enhancement of blueshift, line width, and χ_r^2. However, the blueward asymmetry is clearly not only present at the AR edges, but also existing in other plage/loop footpoint regions. For example, the tongue-like patch ($x = -230''$, $y = -430''$) of blueward asymmetries in Figure 7(h) seems to be coincident with moss and it is not a typical outflow region. The fact is that simple magnetic field structures which are aligned with the line of sight are often not present in AR cores so that the secondary component there is often not revealed as clear blueward asymmetries of line profiles. An obvious correlation between the Doppler shift/Gaussian width derived from the single-Gaussian fit and the peak relative intensity derived from RB$_P$ asymmetry profiles are found in Figure 8, suggesting that the blueshift and enhanced line width are caused by the high-speed secondary emission component and that the single-Gaussian fit cannot accurately reflect the real physical process here. In the following, only those pixels with obvious blueward asymmetry (the average RB asymmetry in 60–110 km s^{-1} smaller than -0.05) and significant signal-to-noise ratio (larger than five) were selected. Clearly, such a cutoff excludes the analysis of spectra in the AR core and edges where the magnetic field lines make large angles relative to the line of sight. The peak relative intensity, velocity, and $1/e$ width derived from RB$_P$ asymmetry profiles of Fe XIV 274.20 Å at these pixels are shown in Figures 7(e)–(g).

The distributions of these three parameters are shown as the red histograms in Figures 11(a)–(c) and they are very similar to those in Figure 6. The only obvious difference is perhaps the slightly larger peak velocity and Gaussian width. In the 2007 January 18 observation, the velocity and width peak at ~75 km s^{-1} and ~50 km s^{-1}, respectively. But in the 2010 September 16 observation, the velocity peaks at ~85 km s^{-1} and the width peaks at ~60 km s^{-1}. The major part of the velocity distribution is still on the left side of 100 km s^{-1} in the 2010 September 16 observation, which is not consistent with the scenario of a considerably broader secondary component (Peter 2010). The scenario of a considerably narrower secondary component can also be excluded since the RB$_P$ width is almost always larger than 35 km s^{-1}. Similar to the 2007 January 18 observation, the RB$_P$ velocity in this recent observation also seldom reaches higher than 150 km s^{-1}, indicating that the line-of-sight velocity of the secondary component is unlikely to be as high as 200 km s^{-1} in this observation. So with the RB asymmetry analysis (particularly RB$_P$), we can conclude that the secondary emission component, which is usually less than 20% and often a few percent of the primary one in intensity, has a speed around ~80 km s^{-1} and a width comparable to the primary component.

4.2. Double-Gaussian Fit

The same algorithm of the RB$_P$ guided double-Gaussian fit was adopted to the asymmetric profiles obtained in the 2010 September 16 observation. Several examples of the observed and fitted line profiles are presented in Figure 9. In Figure 9(a) we show profiles of four emission lines averaged over region 1, which is marked in Figure 7. Blueward asymmetries and deviations from single-Gaussian profiles are clearly present in all four lines. The double-Gaussian algorithm yields a reasonably good fit to the observed spectra. This spatial average is necessary because individual profiles of the Si VII 275.35 Å and Si X 258.37 Å lines are too noisy to allow reliable Gaussian fits and RB asymmetry analysis in the AR boundaries.

We find that the relative intensity and velocity of the secondary component stay relatively stable across the temperature range of $\log(T/\mathrm{K}) = 5.8$–6.3, consistent with the scenario of multi-thermal high-speed upflows, as suggested by our previous work (De Pontieu et al. 2009, 2011; De Pontieu & McIntosh 2010; McIntosh & De Pontieu 2009a, 2009b; McIntosh et al. 2010, 2011; Tian et al. 2011a, 2011b; Martínez-Sykora et al. 2011). The clear presence of blueward asymmetry of the cool Si VII 275.35 Å line is consistent with the finding of McIntosh & De Pontieu (2009a). Compared to other lines, the Si VII 275.35 Å line reveals a smaller velocity (~70 km s^{-1}) of the secondary component. One possible reason could be that the Si VII 275.35 Å line reflects emission from much cooler plasmas so that its line profiles are complicated by cooling downflows (see also Ugarte-Urra & Warren 2011).

Fe XIV 274.20 Å line profiles at four single pixels (without spatial average) are presented in Figures 9(b)–(e). The secondary component resolved by the double-Gaussian fit has different relative intensity and velocity. The magnitude of velocity is likely to be related to the viewing angle of the upflows. If the magnetic field lines associated with the upflows make a

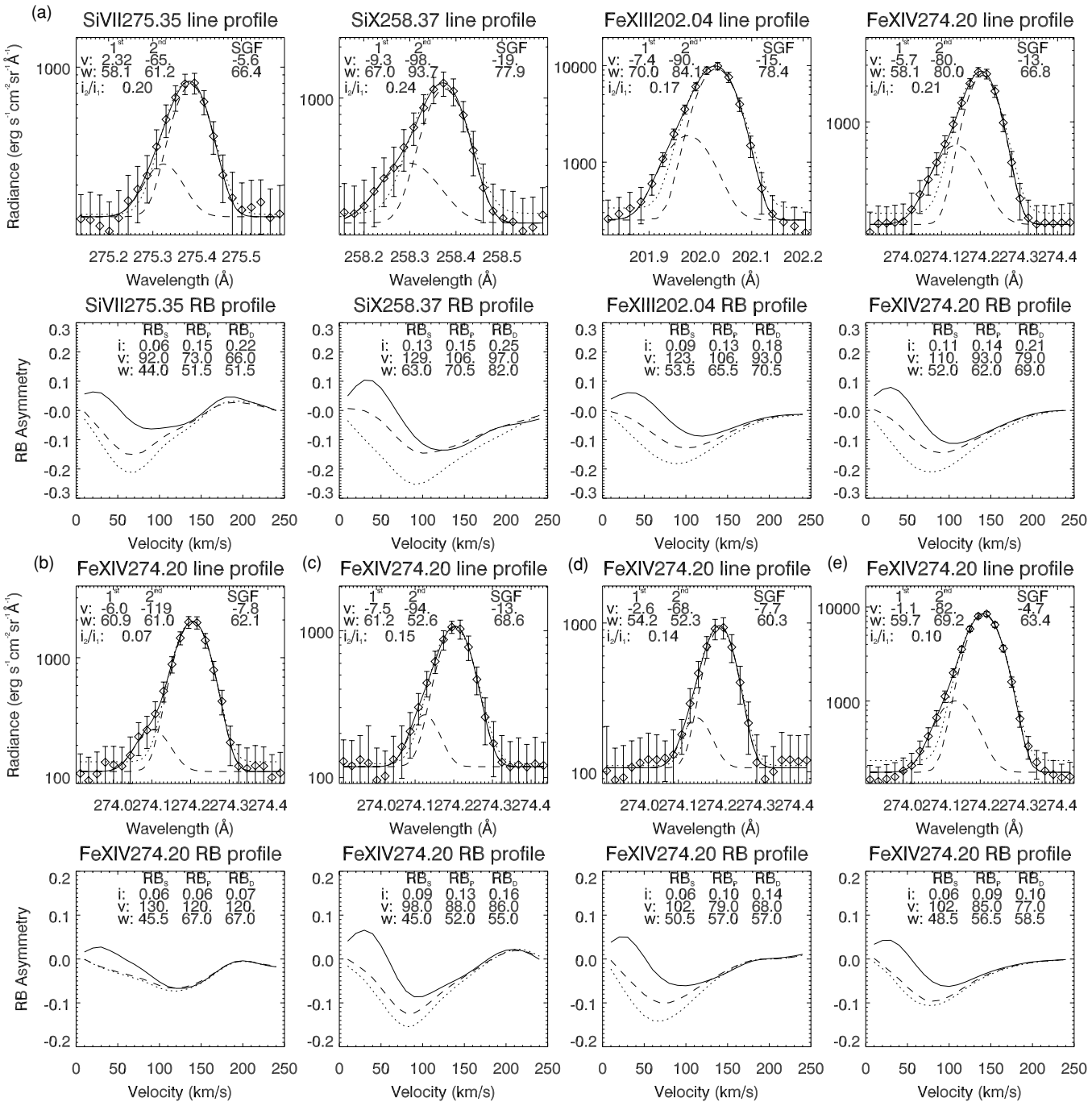

Figure 9. (a) RB asymmetry profiles (bottom) of four emission line profiles (top) averaged in the square marked in Figure 7(a). (b)–(e) RB asymmetry profiles (bottom) of the Fe XIV 274.20 Å line profiles (top) at locations 2–5 marked in Figure 7(a). The line styles and denotations of parameters are the same as in Figure 4.

smaller angle with respect to the line of sight, the observed velocity should be closer to the real velocity. The location of the profile presented in Figure 9(b) is in a weak emission region surrounded by hot loops. This weak emission region might be related to less compact (larger) loops or open field lines which are usually more vertical at lower heights compared to compact and smaller loops. This may explain the large value of velocity ($\sim$120 km s^{-1}). The Gaussian widths of the two components are generally comparable in all these four cases.

The RB_D profiles were then calculated by taking the velocity of the primary component as the line centroid. In Figure 9, we also show the three RB asymmetry profiles (RB_S, RB_P, and RB_D) for the corresponding spectra. The parameters of the secondary component obtained through RB_P and RB_D techniques are usually close to those obtained by using the double-Gaussian fit.

The RB_P guided double-Gaussian fit and RB_D analyses were then applied to all spectra of Fe XIV 274.20 Å with obvious blueward asymmetries. Figure 10 shows the spatial distributions of the three Gaussian parameters of both components as well as the intensity ratio and velocity difference of the two components. Again, we found that the primary component is usually slightly blueshifted by $\sim$10 km s^{-1} in this observation. The velocity of the secondary component is blueshifted by much larger values. The maps of parameters derived from RB_D asymmetry profiles are very similar to those derived from RB_P, which

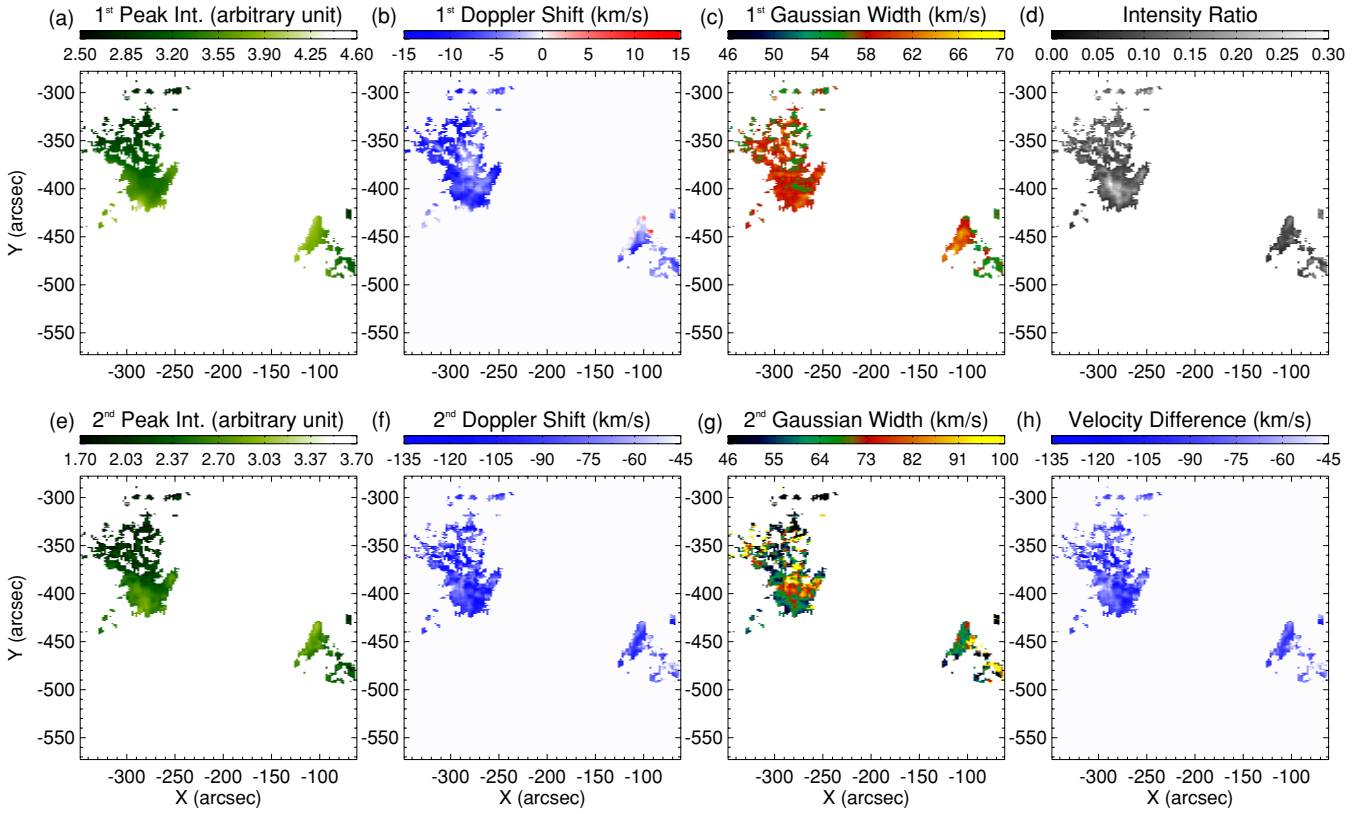

Figure 10. Same as Figure 5 but for the observation on 2010 September 16.
(A color version of this figure is available in the online journal.)

have been presented in Figure 7 and thus are not shown here. Structures on the maps of RB_P peak relative intensity, velocity, and width shown in Figure 7 generally coincide with those on the maps of intensity ratio, velocity difference, and secondary component width as presented in Figure 10, indicating that both the RB_P technique and RB_P guided double-Gaussian fit are able to extract the parameters of the secondary component.

Figures 11(a)–(c) show the distributions of the intensity ratio (relative intensity), velocity difference (velocity), and Gaussian width of the secondary component as derived from double-Gaussian fit and RB asymmetry analyses (RB_P, RB_D). For each of the parameters, the three histograms are very similar. All these histograms show no large difference from those presented in Figure 6, except the slightly larger peak velocity and width. The velocity of the secondary component is usually in the range of 50–120 km s^{-1} in this observation, which is about twice as high as that suggested by Peter (2010).

The distribution of the χ_r^2 ratio between the double- and single-Gaussian fits in Figure 11(d) is also very similar to that in Figure 6(d). The ratio is usually less than 0.5, indicating a significant improvement of the fitting by using the double-Gaussian fit instead of the single-Gaussian fit.

4.3. AIA Observations

During the EIS scan, the AIA instrument took full-disk images of the Sun in several EUV channels at a cadence of 12 s. We selected images in the passbands of 171 Å, 193 Å, and 211 Å for our analysis. The dominant emission of these passbands has a temperature around 0.8 MK, 1.3 MK, and 2 MK, respectively. There were a few missing frames in each passband so that a linear interpolation was applied to the data. The pixel size is about 0.″6.

We extracted a sub-region enclosing the AR observed by EIS and co-aligned different image frames. A movie of AIA 193 Å images and the running difference images is available online (AIA193.mpeg). Figure 12(a) shows an image of AIA 193 Å at 12:06. The rectangle indicates the region scanned by EIS. The cross correlation technique was used to co-align AIA 193 Å and EIS Fe XIV 274.20 Å.

Upward PDs are clearly present in the AIA movie. These disturbances are mainly found at the two boundaries of the AR and coincide with obvious blueward asymmetries as seen from Figure 7(h), suggesting a connection of the two. The speed of these disturbances can be estimated by placing a virtual slit along the propagation direction of the disturbances and calculating the slope of a bright strip in the space–time (S–T) plot (e.g., Sakao et al. 2007; McIntosh et al. 2010; Tian et al. 2011b). Figures 12(b)–(g) show the S–T plots of the original and detrended intensities for the dotted line shown in Figure 12(a). The detrended intensities were used to better reveal the faint outflow signatures and they were obtained by first subtracting an eight-minute running average from the original intensity time series and then normalized to the running average at each location of the slit. One example of PD is indicated by the inclined dashed line. The speed of this PD, the slope of the dashed line, is estimated to be 91 km s^{-1}.

As the PDs are usually present at different passbands of AIA, in principle we should be able to compare the speed of a certain PD at different temperatures using AIA data. For a certain virtual slit, we often find similar patterns of the S–T plots (both the original and detrended intensities) in the 193 Å passband and

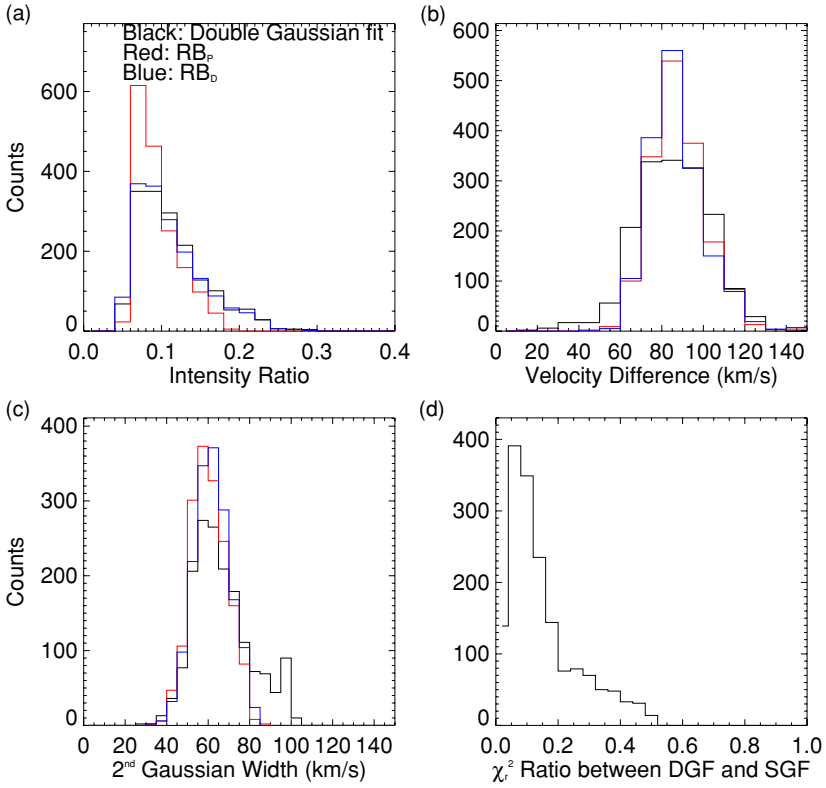

Figure 11. Same as Figure 6 but for the observation on 2010 September 16.
(A color version of this figure is available in the online journal.)

the other two passbands (particularly the 211 Å passband). In most cases, we did not find an obvious increasing trend in the speed with increasing temperature, which seems to support the interpretation of PDs as multi-thermal high-speed upflows (e.g., Sakao et al. 2007; McIntosh & De Pontieu 2009a; De Pontieu & McIntosh 2010; Tian et al. 2011a) rather than slow-mode waves (e.g., De Moortel et al. 2000, 2002; Robbrecht et al. 2001; King et al. 2003; McEwan & De Moortel 2006; Marsh et al. 2009, 2011; Wang et al. 2009a, 2009b; Verwichte et al. 2010; Stenborg et al. 2011). However, a recent investigation suggests that non-dominant cool ions such as O v may contribute significantly to the total emission of the 193 Å and 211 Å passbands (J. Martínez-Sykora et al. 2011, in preparation). But cool ions such as O v would not be expected to show obvious emission over a large height range. For example, PDs are also seen off-limb in a coronal hole up to heights of 50–100 Mm with AIA (Tian et al. 2011b), i.e., heights where emission from cool lines does not typically occur at sufficient strength. This renders the impact of non-dominant cool ions less likely. However, we cannot rule out the possibility of slow waves. Perhaps both slow waves and upflows exist in our observations. In fact, waves can be exited by high-speed flows. But our EIS result that lines with different formation temperatures basically show similar velocities seems to suggest that upflows dominate the emission. We note that for some virtual slits the S–T plots show some differences in different AIA passbands, especially between the 171 Å passband and the other two passbands. The emission in the 171 Å passband is dominated by Fe IX 171.107 Å (O'Dwyer et al. 2010), which is formed in the upper transition region and thus may have a smaller scale height compared to the hotter emission in the other two passbands. Moreover, due to the different sensitivity, signal-to-noise ratio, and emission contrast in different passbands, we may not always be able to clearly identify every outflow event in all the three passbands from the S–T plots. The 211 Å passband samples plasma with a temperature much closer to the formation temperature of Fe XIV 274.20 Å. However, the 211 Å images have a lower signal-to-noise ratio and are thus noisier compared to the 193 Å images. Since the S–T plots in the 211 Å passband are highly similar to those in the 193 Å passband, in the following we concentrate on the 193 Å images.

We identified 39 well-isolated disturbances propagating along the fan-like structure at the left boundary of the AR and calculated their propagating speeds in the 193 Å passband. A speed distribution was then obtained. A comparison of this speed distribution with the distribution of the velocities derived from EIS Fe XIV 274.20 Å line profiles (through double-Gaussian fit, RB_P, and RB_D analyses) is presented in Figures 13(a) and (b). Here only line profiles with obvious blueward asymmetries in the fan-like structure at the left boundary of the AR were used. By using the potential field source surface (PFSS) model (Schatten et al. 1969; Schrijver & DeRosa 2003), the inclination angles of the magnetic field lines in the fan-like structure at the left boundary of the AR were estimated to be around 55° with respect to the line of sight. Disturbances propagating at a speed of V along these magnetic field lines should exhibit a plane-of-sky speed of $V \sin 55°$ and a line-of-sight speed of $V \cos 55°$. The ratio of the two speed components is 1.43. Since the speeds derived from S–T plots of AIA images are the real speeds projected onto the plane of sky and the speeds derived from EIS line profiles are the line-of-sight component of the real speeds, the ratio of the two should be around 1.43. From Figure 13 we find that this is indeed the case. The speeds derived by using AIA data are systematically larger than those derived by using EIS data. The ratio of the two average speeds is around

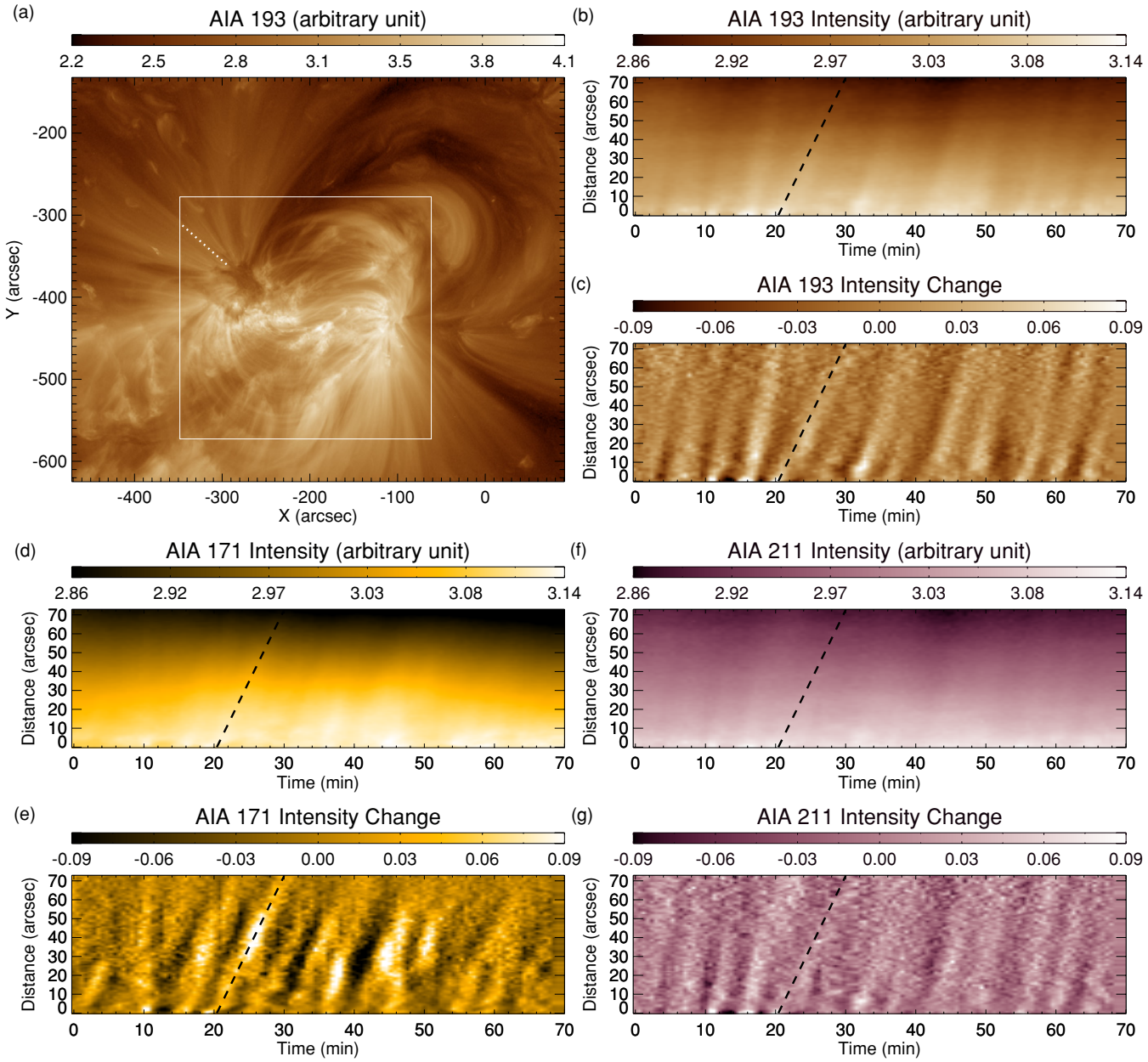

Figure 12. (a) The image of AIA 193 Å at 12:06 on 2010 September 16. The rectangle outlines the region scanned by EIS. (b) A space–time plot of the AIA 193 Å intensity for the dotted line shown in (a). (c) Same as (b) but showing the detrended intensity. (d and e) Same as (b) and (c) but for AIA 171 Å. (f and g) Same as (b) and (c) but for AIA 211 Å. The inclined dashed line indicates one propagating disturbance with a traveling speed of about 91 km s^{-1}. A movie associated with (a) is available online (AIA193.mpeg).

(An animation and a color version of this figure is available in the online journal.)

$135/85 = 1.58$, which is close to 1.43. For comparison, the RB_P velocity histogram is multiplied by 1.58 and overplotted as the dotted line in Figure 13(b). The small difference between 1.58 and 1.43 could easily be caused by the fact that the PFSS model is not expected to give a perfect representation of what viewing angles the real Sun presents. We think that in the future three-dimensional reconstruction (e.g., Feng et al. 2007; Aschwanden et al. 2008) could be considered as an alternate method to help relate the velocities derived from imaging and spectroscopic observations. In Figure 13, we can also compare histograms of the relative intensities derived from EIS Fe XIV 274.20 Å line profiles (in panel (c), through double-Gaussian fit, RB_P, and RB_D analyses) and those derived from S–T plots (d). The latter were obtained through the following process: we first smoothed the original time series with a one-hour kernel. After that we subtracted the smoothed time series from the original one and obtained a time series of intensity change. The relative intensity was then obtained by normalizing the maximum intensity change to the average intensity at each slit location. From Figure 13(d), we can see that the relative intensity is usually a few percent but can also be larger than 10%, which is consistent with the magnitude of the relative intensity of the secondary component revealed by RB asymmetry analysis and double-Gaussian fit. For a better comparison, the RB_P relative intensity histogram is overplotted as the dotted line in Figure 13(d). Note that the lack of small values of the relative intensity derived from EIS line profiles are due to the fact that we only selected profiles with significant blueward asymmetries. These results provide further support to the argument that the blueward asymmetries of coronal line profiles are caused by the

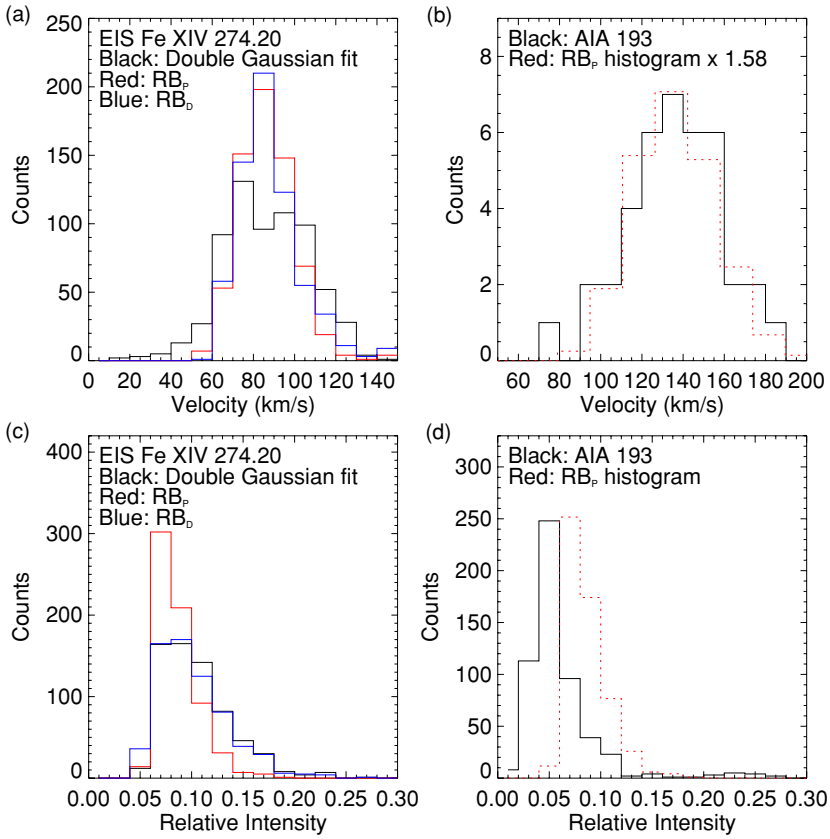

Figure 13. Histograms of the velocity and relative intensity derived from the EIS Fe XIV 274.20 Å line profiles (a, c) and AIA 193 Å S–T plots (b, d) in the fan-like region at the left boundary of NOAA AR 11106. In (a) and (c) the black, red, and blue histograms represent results of the double-Gaussian fit, RB_P, and RB_D analyses, respectively. For comparison, the RB_P velocity histogram is multiplied by 1.58 and overplotted as the dotted line in (b), and the RB_P relative intensity histogram is overplotted in (d) as the dotted line.

(A color version of this figure is available in the online journal.)

upward PDs at AR boundaries (McIntosh & De Pontieu 2009a; Tian et al. 2011a).

As mentioned by De Moortel (2009), although there are striking similarities, it is not clear how the outflows inferred from EIS line profiles and the PDs seen in EUV imaging observations are related. De Moortel (2009) pointed out that the blueshifts (from a single-Gaussian fit) of EIS lines are only of the order of 20–50 km s^{-1} and no periodicity has been reported. Yet the PDs in imaging observations have a speed of ~100 km s^{-1} and they are often quasi-periodic. Now we understand that the EIS line profile consists of two components and that the secondary component has a velocity of ~100 km s^{-1}. And we have already demonstrated that the secondary component is also quasi-periodically enhanced or weakened (De Pontieu & McIntosh 2010; Tian et al. 2011a). The consistency between properties of the PDs observed by AIA and those of the secondary component revealed by RB asymmetry analysis and double-Gaussian fit of EIS line profiles suggests a close connection of the two. It is thus natural to suggest that the PDs are responsible for the blueward asymmetries of line profiles. The non-thermal width of the secondary component is probably caused by both the superposition of multiple unresolved upflows and the Alfvénic motions associated with the upflows (McIntosh & De Pontieu 2009a; Dolla & Zhukov 2011).

We have to mention that in Figure 13 we only present the results for the fan-like structure at the northeast boundary of the AR because of the simple magnetic field structure there. From the online movie (AIA193.mpeg), we can see that outward PDs are also clearly present in the fan-like structure to the southwest of the AR. We produced several S–T plots and found generally similar S–T patterns in different passbands. However, the footpoints of these fan loops (around $x = -110''$, $y = -450''$) are mixed together and the higher parts of different loops are not well separated, making it difficult to identify well-isolated PDs in the S–T plots. In other parts of the AR, magnetic field structures are either too complex or only slightly inclined with respect to the line of sight so that reliable speeds may not be obtained through S–T plots.

5. CONCLUSION

In conclusion, the presence of asymmetric coronal line profiles in loop footpoint regions suggests that at least two emission components are present: an almost stationary primary component and a high-speed secondary component. The secondary emission component might play an important role in supplying the corona with hot plasma. We have shown that the significant blue shift and enhanced line width derived from a single Gaussian fit are actually caused by the superposition of the two components, implying that previous results and suggestions based on a single Guassian fit, e.g., slow solar wind origin from AR boundaries at a speed of 20–50 km s^{-1} (Sakao et al. 2007; Harra et al. 2008; Doschek et al. 2008; Brooks & Warren 2011), might need to be reconsidered.

We have generated artificial spectra composed of two Gaussian components to test the ability of extracting the Gaussian parameters (intensity, velocity, and width) of the secondary component through the originally defined (use the

single-Gaussian fit to determine the line centroid) and a slightly modified (use the spectral position corresponding to the peak intensity as the line centroid) technique of the RB asymmetry analysis. We find that this technique, especially the modified one, can provide a relatively accurate estimate of the parameters of the secondary component if the velocity is larger and the width is not considerably larger than the primary component width. We have applied the modified technique to the spectra obtained by the EIS instrument on board *Hinode* in two ARs and found that the distributions of the velocity/width determined from the RB asymmetry analysis peak around 80 km s^{-1}/60 km s^{-1}. A comparison of such distributions with the values of velocity/width calculated from the artificial spectra suggests that the secondary component cannot be very broad or narrow and that the widths of the two components are comparable. The velocity of the secondary component is usually within the range of 50–150 km s^{-1} and seldom reaches as high as 200 km s^{-1} or as low as 40 km s^{-1} in our EIS observations. The relative intensity of the secondary component with respect to the primary one is often a few percent but can sometimes reach 30%. Our conclusions are very different from those of Peter (2010), who claimed that the secondary component contributes some 10%–20% to the total emission, is about twice as broad as the primary component, and is blueshifted by up to 50 km s^{-1}. The velocity range of the secondary component we derived here is roughly consistent with yet slightly smaller than that derived by Bryans et al. (2010). However, we find that the very high speed of 200 km s^{-1} mentioned by Bryans et al. (2010) seems to be not very likely.

Using the parameters determined from the RB asymmetry analysis and single-Gaussian fit as initial values for several free parameters, we have performed a double-Gaussian fit to the spectra that were observed to have obvious blueward asymmetries. The RB asymmetry analysis has been performed for the third time, but then using the centroid of the secondary component determined from the double-Gaussian fit as the line centroid. The double-Gaussian fit and the RB asymmetry analyses have given basically consistent results. The properties of the secondary component stay relatively stable across the temperature range of $\log(T/\mathrm{K}) = 5.8$–6.3. The double-Gaussian fit also shows that the velocity of the primary component is often blueshifted by $\sim$10 km s^{-1}.

We have also used imaging observation simultaneously performed by the AIA instrument on board *SDO* and demonstrated that the PDs coincide with obvious blueward asymmetries of line profiles, and show an intensity change similar to the relative intensity of the secondary component of line profiles and an average velocity consistent with that derived from emission line profiles. Such results suggest that the upward PDs are plasma upflows responsible for the blueward asymmetries of line profiles. The inconsistency between the outflows inferred from EIS line profiles and the PDs seen in EUV/X-ray imaging observations, as noticed by De Moortel (2009), has thus been solved.

SDO is the first mission of NASA's Living With a Star (LWS) Program. EIS is an instrument on board *Hinode*, a Japanese mission developed and launched by ISAS/JAXA, with NAOJ as domestic partner and NASA and STFC (UK) as international partners. It is operated by these agencies in cooperation with ESA and NSC (Norway). S.W.M. is supported by NASA (NNX08AL22G, NNX08BA99G) and NSF (ATM-0541567, ATM-0925177). B.D.P. is supported by NASA grants NNX08AL22G and NNX08BA99G. H.T. is supported by the ASP Postdoctoral Fellowship Program of NCAR. The National Center for Atmospheric Research is sponsored by the National Science Foundation. H.T. thanks Marc DeRosa for his assistance in using the PFSS package. We appreciate the efforts of the referee to improve the manuscript.

APPENDIX A

A COMPARISON BETWEEN RB_P AND RB_S RESULTS

As we mentioned in Section 2, both the RB_P and RB_S techniques can provide a relatively accurate estimate of the Gaussian parameters of the secondary component when the offset velocity is larger than the Gaussian width of the primary component. We have also found that the modified RB technique, RB_P, has a better ability to accurately quantify the properties of the secondary component as compared with the originally defined RB_S technique. Figure 14 shows a comparison between the RB_P and RB_S results for the 2010 September 16 observation. We can see that the spatial structures in all of the four parameters are very similar. The most prominent difference is the smaller values of relative intensity and width, and larger upflow velocity for RB_S. Such results are fully consistent with our forward modeling results in Figure 1 and imply that in our previous work the relative intensity and width might be underestimated while the upflow velocity was likely slightly overestimated.

APPENDIX B

A COMPARISON BETWEEN EIS Fe XIV 274.20 Å AND Fe XIV 264.78 Å LINE MOMENTS AND PROFILE ASYMMETRIES

We have mentioned that the strong Fe XIV 274.20 Å line is blended with the weak Si VII 274.18 Å line and that the latter can safely be ignored in AR conditions (Young et al. 2007). The very close wavelengths (about one spectral pixel) of the two also suggest that the blend is very unlikely to have an important impact on the high-speed (of the order of 100 km s^{-1}) upflow. The Fe XIV 264.78 Å line spectra were not obtained in the 2007 January 18 observation so we cannot provide a direct comparison of it with the Fe XIV 274.20 Å line. In 2010 September 16, both Fe XIV lines were used in the observation and Figure 15 shows the spatial distributions of the line moments and profile asymmetries. Note that the spectra (especially for the Fe XIV 264.78 Å line) in the upper left corner, the higher part of the fan, have low signal-to-noise ratio and thus the line moments and profile asymmetries are noisy there. The very similar behavior of line moments and profile asymmetries between Fe XIV 274.20 Å and the weaker but clean Fe XIV 264.78 Å line provides further confidence that the blend of Si VII 274.18 Å line can be safely ignored in our analysis.

APPENDIX C

EIS OBSERVATION ON 2007 DECEMBER 12

We also applied the techniques of RB asymmetry analysis and double-Gaussian fit to an EIS observation of AR NOAA 10978 from 11:43 to 17:03 on 2007 December 12. Bryans et al. (2010) found that the secondary emission component in this AR has velocities around 110 km s^{-1} and, as they stated in their paper, often as high as 200 km s^{-1}. Bryans et al. (2010) used the Fe XII 195.12 Å line and they mentioned that the blend of this line, Fe XII 195.18 Å, should not significantly affect the Fe XII 195.12 Å line in the low-density (Doschek et al. 2008; Brooks & Warren 2011) outflow region (AR edges). However,

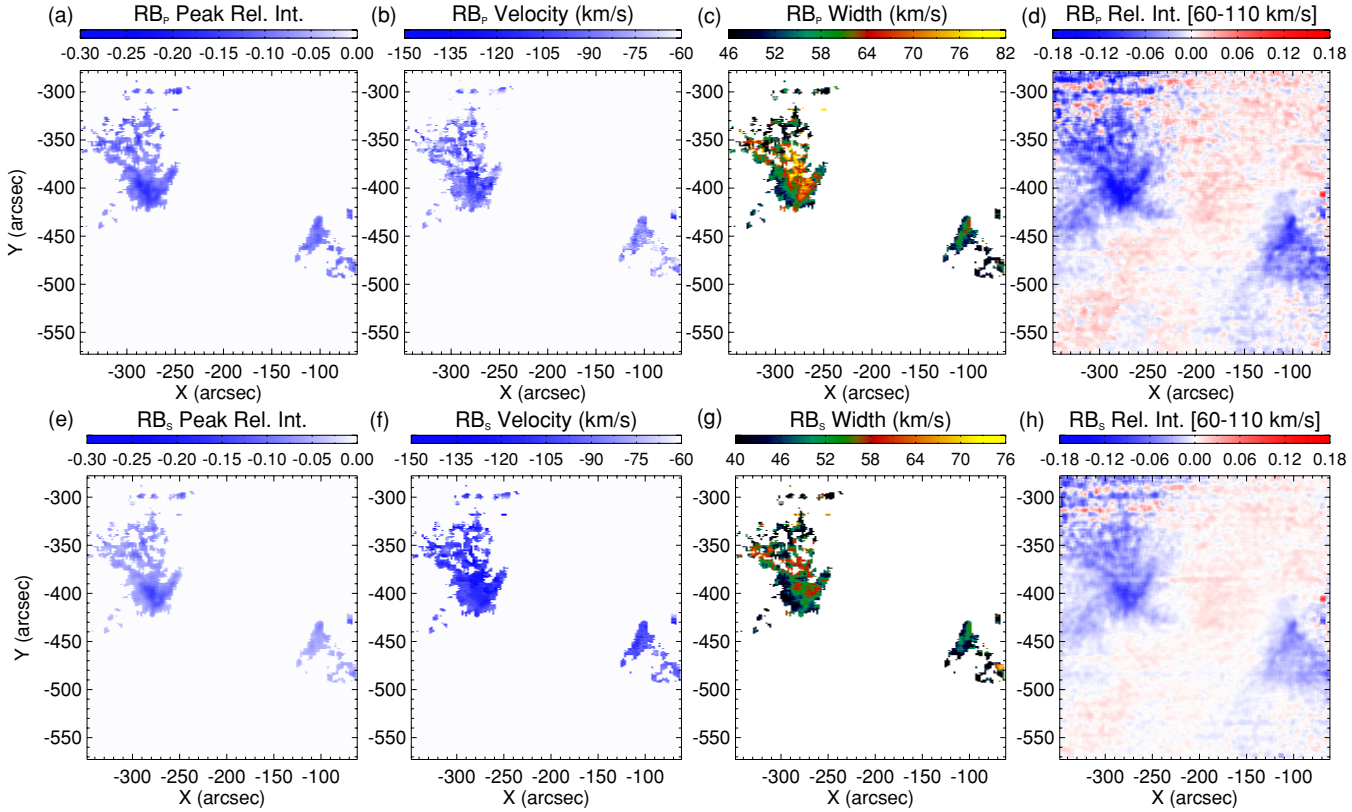

Figure 14. Spatial distributions of the parameters derived from RB_P (a–d) and RB_S (e–h) asymmetry analyses for Fe XIV 274.20 Å in the observation on 2010 September 16.

(A color version of this figure is available in the online journal.)

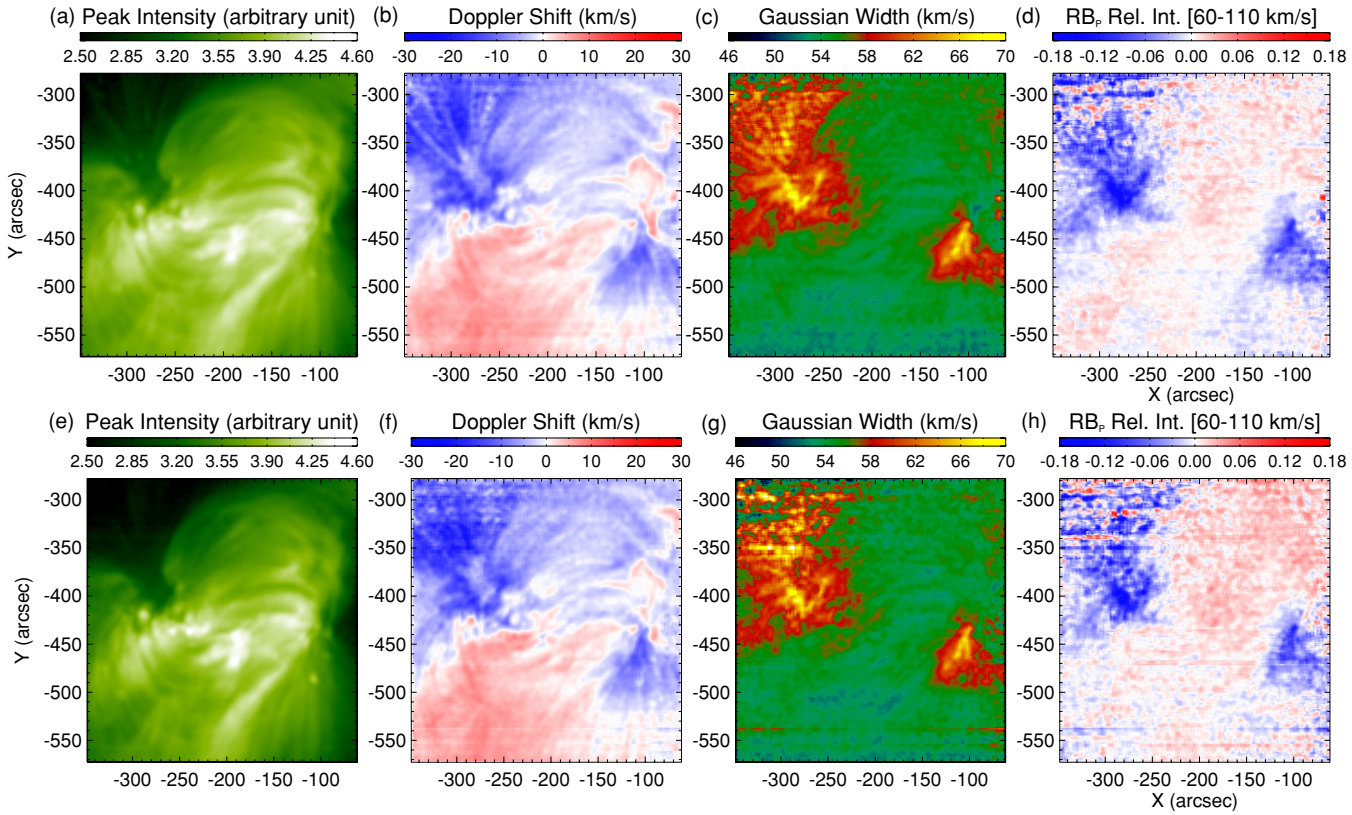

Figure 15. Spatial distributions of the line moments (single-Gaussian parameters) and profile asymmetries (average relative intensity in the velocity interval of 60–110 km s^{-1}, as obtained from the RB_P profiles) for Fe XIV 274.20 Å (a–d) and Fe XIV 264.78 Å (e–h) in the observation on 2010 September 16.

(A color version of this figure is available in the online journal.)

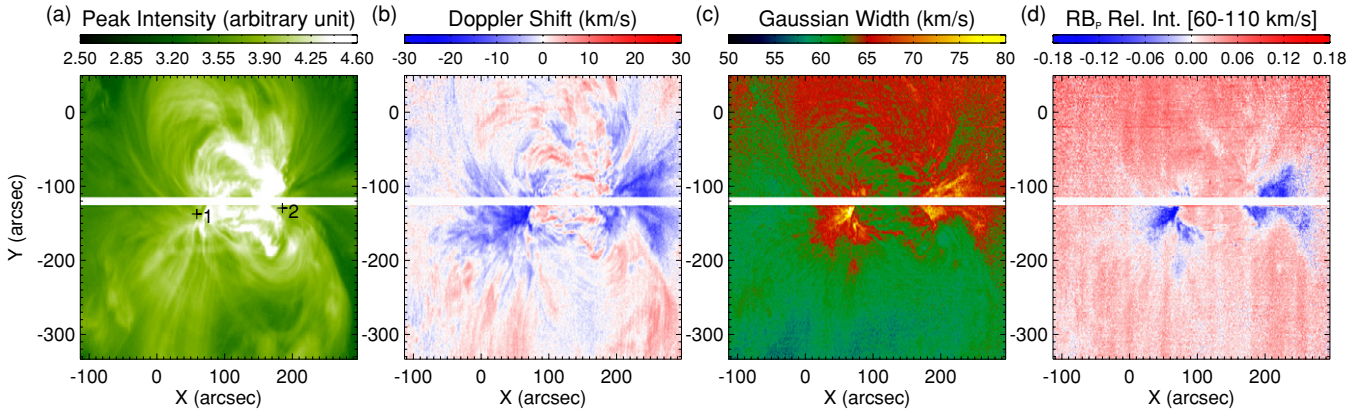

Figure 16. Spatial distributions of single-Gaussian parameters and profile asymmetries (average relative intensity in the velocity interval of 60–110 km s^{-1}, as obtained from the RB$_P$ profiles) for Fe XII 193.51 Å in the observation on 2007 December 12. The two pluses mark locations of the line profiles presented in Figures 17(a) and (b), respectively.

(A color version of this figure is available in the online journal.)

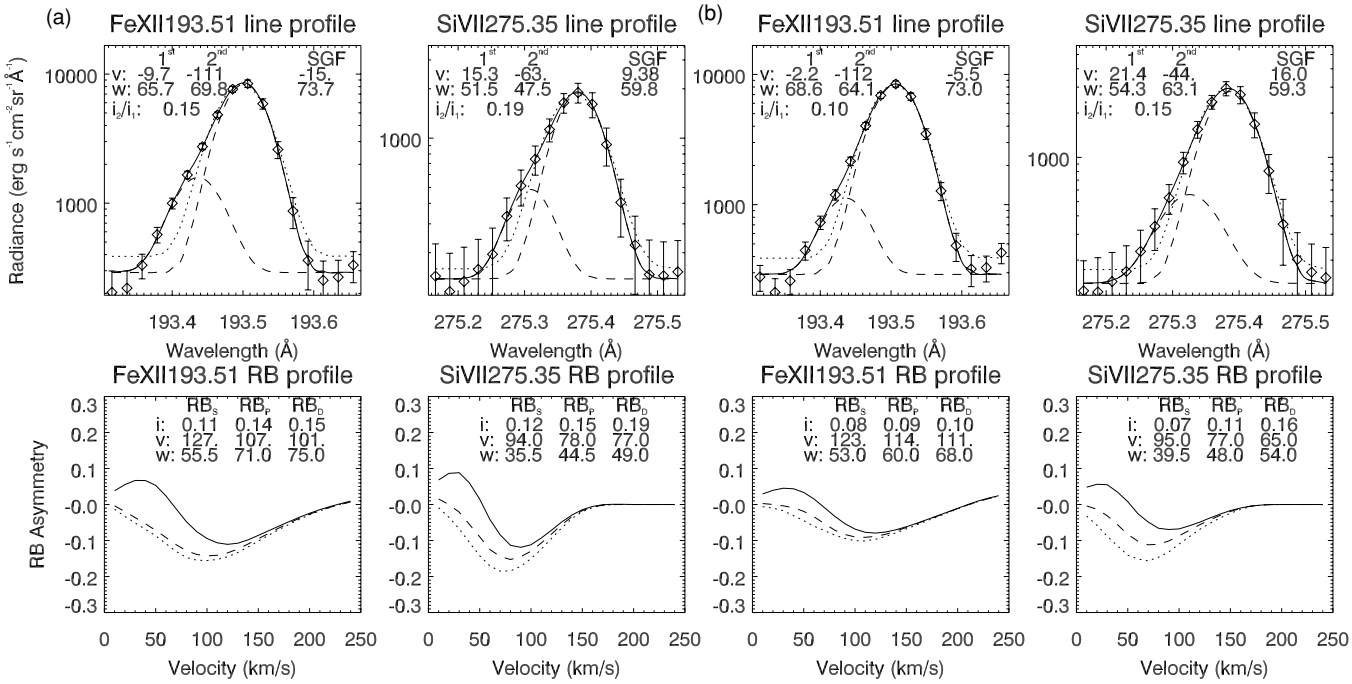

Figure 17. (a) RB asymmetry profiles of the Fe XII 193.51 Å and Si VII 275.35 Å line profiles at location 1 marked in Figure 16(a). The line styles and denotations of parameters are the same as in Figure 4. (b) Same as (a) but for the line profiles at location 2 marked in Figure 16(a).

to avoid the complexity introduced by this blend we decided to turn to other clean and strong Fe XII lines. We found that in the AR edges some other lines at the far blue wing of the Fe XII 192.39 Å line can be relatively strong and thus affect the results of RB asymmetry analysis and double-Gaussian fit. So here we mainly present the results of the Fe XII 193.51 Å line, which is clean and about two-third as strong as Fe XII 195.12 Å. Since the line is very strong, there is no need to perform a spatial average of the line profiles.

Figure 16 shows the spatial distributions of the single-Gaussian parameters and profile asymmetry. Similar to AR 10938 and AR 11106, the two loop footpoint regions are characterized by an enhancement in the blueshift, line width, and blueward profile asymmetry, and there is an obvious correlation between the Doppler shift/Gaussian width and profile asymmetry. Note that the white strip in each panel mark locations where the observed data are lost.

Two examples of line profiles and the corresponding RB asymmetry profiles of the Fe XII 193.51 Å and Si VII 275.35 Å lines are shown in Figure 17. The profiles were averaged over three pixels centered at the locations marked in Figure 16(a) in both spatial dimensions. Bryans et al. (2010) mentioned that cool lines like Si VII 275.35 Å do not have any significant asymmetries and that their profiles can be accurately represented by a single Gaussian. We found that this is not always the case. Similar to what we found in AR 11106, at some locations the Si VII 275.35 Å line profiles clearly exhibit obvious asymmetries. As shown in Figure 17, usually the primary component is redshifted by ∼15 km s^{-1} and the velocity difference between the two components is smaller than that of Fe XII 193.51 Å, which might be due to the complexity introduced by cooling downflows.

Similar to what we did for AR 10938 and AR 11106, the techniques of RB asymmetry analysis and RB$_P$ guided

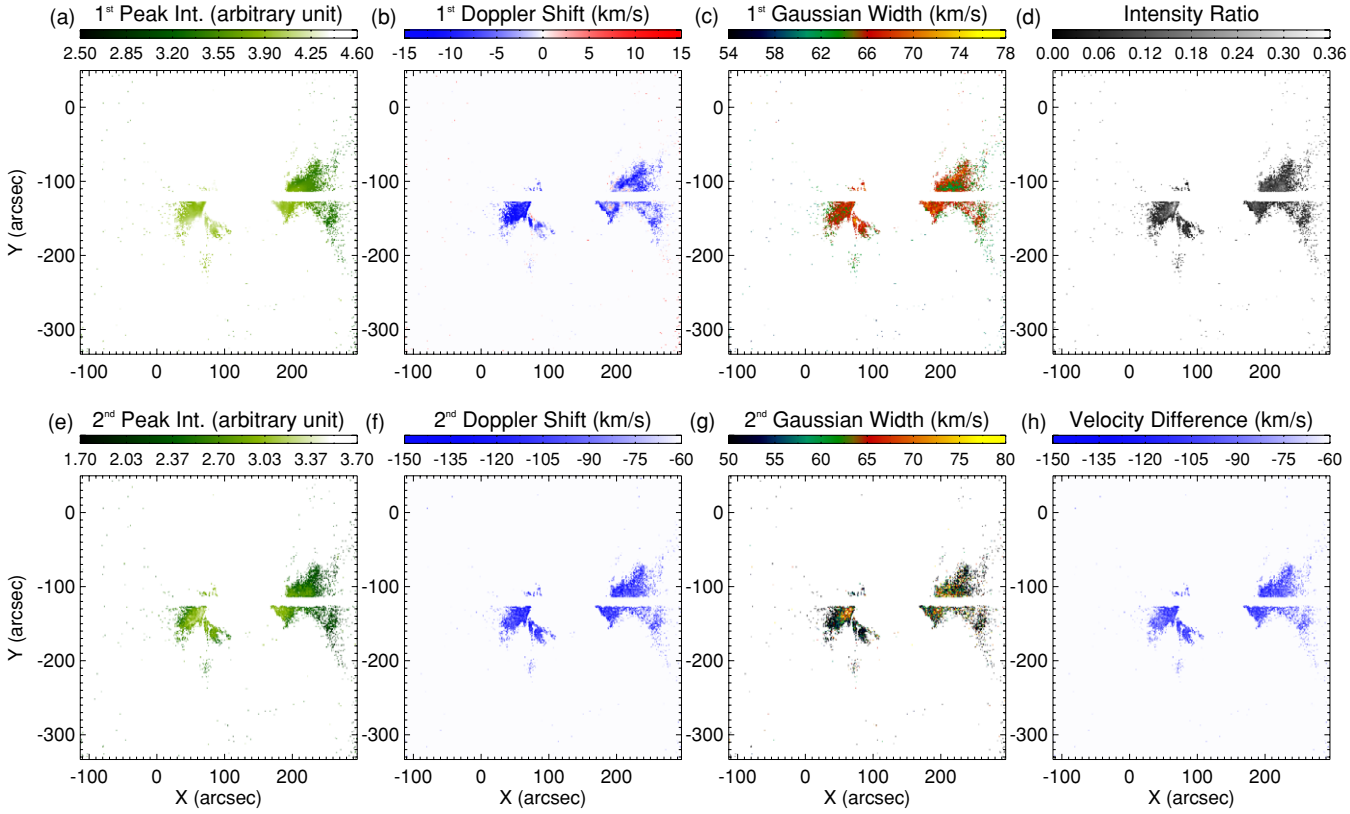

Figure 18. Same as Figure 5 but for the observation on 2007 December 12.
(A color version of this figure is available in the online journal.)

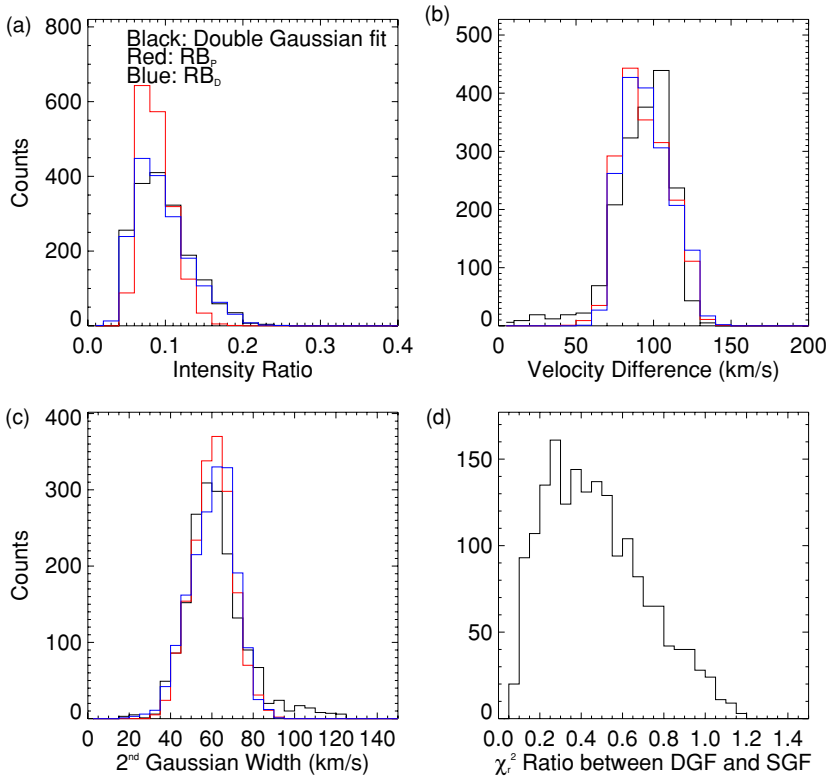

Figure 19. Same as Figure 6 but for the observation on 2007 December 12.
(A color version of this figure is available in the online journal.)

double-Gaussian fit were applied to each spectral profile with an obvious blueward asymmetry (the average RB asymmetry in 60–110 km s^{-1} smaller than −0.05). Spatial distributions of the double-Gaussian parameters are presented in Figure 18. Spatial distributions of the Gaussian parameters derived from the RB_P and RB_D analyses are similar to those of the secondary component shown in Figure 18, and thus are not shown here.

The distributions of the intensity ratio (relative intensity), velocity difference (velocity), and Gaussian width of the secondary component as derived from double-Gaussian fit and RB asymmetry analyses (RB_P, RB_D), as shown in Figures 19(a)–(c), reveal no big difference from those in Figure 11. However, the velocity distributions seem to peak at ∼95 km s^{-1}, a value larger than those in AR 10938 (∼75 km s^{-1}) and AR 11106 (∼85 km s^{-1}) and close to that derived by Bryans et al. (2010; ∼110 km s^{-1}). The velocity seldom reaches as high as 200 km s^{-1}. In fact, from Figure 7 of Bryans et al. (2010) one can conclude that the velocity of the secondary component is usually in the range of 60–170 km s^{-1} and that only a very minor portion of the velocities exceeds 200 km s^{-1}.

As seen from Figure 19(d), the χ_r^2 ratio between the double- and single-Gaussian fits is generally smaller than 1, indicating an improvement of the fitting by using the double-Gaussian fit instead of the single-Gaussian fit.

REFERENCES

Aschwanden, M. J., Wülser, J.-P., Nitta, N. V., & Lemen, J. R. 2008, ApJ, 679, 827
Banerjee, D., Pérez-Suárez, D., & Doyle, J. G. 2009, A&A, 501, L15
Banerjee, D., Teriaca, L., Doyle, J. G., & Wilhelm, K. 1998, A&A, 339, 208
Bevington, P. R., & Robinson, D. K. 1992, Data Reduction and Error Analysis for the Physics Sciences (New York: McGraw-Hill)
Brooks, D. H., & Warren, H. P. 2011, ApJ, 727, L13
Brown, C. M., et al. 2008, ApJS, 176, 511
Bryans, P., Young, P. R., & Doschek, G. A. 2010, ApJ, 715, 1012
Culhane, J. L., et al. 2007, Sol. Phys., 243, 19
Del Zanna, G. 2008, A&A, 481, L49
Del Zanna, G., Aulanier, G., Klein, K.-L., & Török, T. 2011, A&A, 526, A137
De Moortel, I. 2009, Space Sci. Rev., 149, 65
De Moortel, I., Ireland, J., Hood, A. W., & Walsh, R. W. 2002, A&A, 387, L13
De Moortel, I., Ireland, J., & Walsh, R. W. 2000, A&A, 355, L23
De Pontieu, B., & McIntosh, S. W. 2010, ApJ, 722, 1013
De Pontieu, B., McIntosh, S. W., Hansteen, V. H., & Schrijver, C. J. 2009, ApJ, 701, L1
De Pontieu, B., et al. 2007, PASJ, 59, S655
De Pontieu, B., et al. 2011, Science, 331, 55
Dolla, L. R., & Zhukov, A. N. 2011, ApJ, 730, 113
Doschek, G. A., et al. 2007, ApJ, 667, L109
Doschek, G. A., et al. 2008, ApJ, 686, 1362
Feng, L., et al. 2007, ApJ, 671, L205
Guo, L. J., Tian, H., & He, J.-S. 2010, Res. Astron. Astrophys., 10, 1307
Hansteen, V. H., Hara, H., De Pontieu, B., & Carlsson, M. 2010, ApJ, 718, 1070
Hara, H., et al. 2008, ApJ, 678, 67
Harra, L. K., et al. 2008, ApJ, 676, L147
He, J.-S., Marsch, E., Tu, C.-Y., Guo, L.-J., & Tian, H. 2010, A&A, 516, A14
Judge, P. G., Tritschler, A., & Low, B. C. 2011, ApJ, 730, L4
King, D. B., et al. 2003, A&A, 404, L1
Lemen, J. R., et al. 2011, Sol. Phys.
Mariska, J. T., & Muglach, K. 2010, ApJ, 713, 573
Marsch, E., Tian, H., Sun, J., Curdt, W., & Wiegelmann, T. 2008, ApJ, 684, 1262
Marsch, E., Wiegelmann, T., & Xia, L. D. 2004, A&A, 428, 629
Marsh, M. S., De Moortel, I., & Walsh, R. W. 2011, ApJ, 734, 81
Marsh, M. S., Walsh, R. W., & Plunkett, S. 2009, ApJ, 697, 1674
Martínez-Sykora, J., De Pontieu, B., Hansteen, V., & McIntosh, S. W. 2011, ApJ, 732, 84
McEwan, M. P., & De Moortel, I. 2006, A&A, 448, 763
McIntosh, S. W., & De Pontieu, B. 2009a, ApJ, 706, L80
McIntosh, S. W., & De Pontieu, B. 2009b, ApJ, 707, 524
McIntosh, S. W., Innes, D. E., De Pontieu, B., & Leamon, R. J. 2010, A&A, 510, L2
McIntosh, S. W., Leamon, R. J., & De Pontieu, B. 2011, ApJ, 727, 7
Murray, M. J., Baker, D., van Driel-Gesztelyi, L., & Sun, J. 2010, Sol. Phys., 261, 253
O'Dwyer, B., Del Zanna, G., Mason, H. E., Weber, M. A., & Tripathi, D. 2010, A&A, 521, A21
Peter, H. 2001, A&A, 374, 1108
Peter, H. 2010, A&A, 521, A51
Raju, K. P. 1999, Sol. Phys., 185, 311
Raju, K. P., Chandrasekhar, T., & Ashok, N. M. 2011, ApJ, in press
Robbrecht, E., et al. 2001, A&A, 370, 591
Rouppe van der Voort, L., Leenaarts, J., De Pontieu, B., Carlsson, M., & Vissers, G. 2009, ApJ, 705, 272
Sakao, T., et al. 2007, Science, 318, 1585
Schatten, K. H., Wilcox, J. M., & Ness, N. F. 1969, Sol. Phys., 6, 442
Schrijver, C. J., & DeRosa, M. L. 2003, Sol. Phys., 212, 165
Stenborg, G., Marsch, E., Vourlidas, A., Howard, R., & Baldwin, K. 2011, A&A, 526, A58
Tian, H., McIntosh, S. W., & De Pontieu, B. 2011a, ApJ, 727, L37
Tian, H., McIntosh, S. W., Habbal, S. R., & He, J.-S. 2011b, ApJ, 736, 130
Tripathi, D., Mason, H. E., Dwivedi, B. N., del Zanna, G., & Young, P. R. 2009, ApJ, 694, 1256
Ugarte-Urra, I., & Warren, H. 2011, ApJ, 730, 37
Verwichte, E., et al. 2010, ApJ, 724, 194
Wang, T. J., Ofman, L., & Davila, J. M. 2009a, ApJ, 696, 1448
Wang, T. J., Ofman, L., Davila, J. M., & Mariska, J. T. 2009b, A&A, 503, L25
Wang, Y.-M., Ko, Y.-K., & Grappin, R. 2009c, ApJ, 691, 760
Warren, H. P., Ugarte-Urra, I., Young, P. R., & Stenborg, G. 2011, ApJ, 727, 58
Young, P. R., et al. 2007, PASJ, 59, S857